Simulations of a Membrane-Anchored Peptide: Structure, Dynamics, and Influence on Bilayer Properties

Morten Ø. Jensen,* Ole G. Mouritsen,[†] and Günther H. Peters[‡]

*Quantum Protein Center, Department of Physics, Technical University of Denmark, Lyngby, Denmark;
[†]Center for Biomembrane Physics (MEMPHYS), Department of Physics, University of Southern Denmark, Odense M, Denmark; and
[‡]Center for Biomembrane Physics (MEMPHYS), Department of Chemistry, Technical University of Denmark, Lyngby, Denmark

ABSTRACT   A three-dimensional structure of a model decapeptide is obtained by performing molecular dynamics simulations of the peptide in explicit water. Interactions between an N-myristoylated form of the folded peptide anchored to dipalmitoylphosphatidylcholine fluid phase lipid membranes are studied at different applied surface tensions by molecular dynamics simulations. The lipid membrane environment influences the conformational space explored by the peptide. The overall secondary structure of the anchored peptide is found to deviate at times from its structure in aqueous solution through reversible conformational transitions. The peptide is, despite the anchor, highly mobile at the membrane surface with the peptide motion along the bilayer normal being integrated into the collective modes of the membrane. Peptide anchoring moderately alters the lateral compressibility of the bilayer by changing the equilibrium area of the membrane. Although membrane anchoring moderately affects the elastic properties of the bilayer, the model peptide studied here exhibits conformational flexibility and our results therefore suggest that peptide acylation is a feasible way to reinforce peptide-membrane interactions whereby, e.g., the lifetime of receptor-ligand interactions can be prolonged.

INTRODUCTION

A central issue in membrane biophysics is the investigation of the energetics of protein/peptide-membrane systems since they are an integral part of many cell processes, including for instance transport, immune response, signal transduction, cell aggregation, membrane fusion, and membrane rupture (Stryer, 1988). Most of our information about peptide/membrane systems stems from a variety of powerful biochemical and biophysical (mainly spectroscopic) experiments providing an insight into the effect of peptides on the phase state and mechanical properties of membranes. However, there is still a gap in relating these macroscopic membrane properties to peptide-membrane interactions occurring at a molecular level. Here, we present a simulation study investigating in detail the effect of an acylated peptide on a lipid membrane and the collective behavior of this complex. Commonly, peptides can interact with the membrane on different levels spanning from simple adsorption onto the membrane surface to insertion into the hydrocarbon core of the membrane. The association of peptides with the hydrophobic core is driven by hydrophobic interactions and partially counterbalanced by the electrostatic free energy penalty resulting from the transfer of polar groups (e.g., peptide backbone) from the aqueous phase into the hydrocarbon region of the membrane (White and Wimley, 1998).

Antimicrobial peptides such as gramicidin, melittin, and alamethicin, all α-helical amphiphatic peptides, are exam-

ples of transmembrane pore-forming peptides that have membrane-perturbing effects (Tieleman et al., 1999; Tieleman and Berendsen, 1998; La Rocca et al., 1999). The resulting channels dissipate, in contrast to other naturally occurring channels, the electrochemical potential across the cell membrane thereby abrogating crucial physiological processes such as ATP synthesis. Related processes at the membrane interface involve adsorption of peptides or proteins to the membrane surface and their specific interaction with the polar headgroup region (Tieleman et al., 1999; Tieleman and Berendsen, 1998; La Rocca et al., 1999; Aliste et al., 2003). Magainin is an example of an α-helical, antimicrobial peptide that might not insert into the membrane but associate noncovalently with the surface of the membrane and thereby affects the mechanical properties of the lipid membrane (La Rocca et al., 1999). Similarly, the neuronal anchoring protein, AKAP79, associates mainly electrostatically with the membrane surface (Dell'Aqua and Scott, 1997; Dell'Aqua et al., 1998). Moreover, several important peripheral proteins are membrane-anchored by a combination of a hydrocarbon chain, which interacts with the hydrophobic core of the bilayer, and a region of positively charged residues that interact (mainly) electrostatically with negatively charged lipids in the membrane (Dell'Aqua et al., 1998; Faux and Scott, 1996). Cytochrome C and protein kinase C, both having a hydrophobic crevice, have been proposed to bind to the membrane surface by the so-called extended lipid anchorage (Tuominen et al., 2002). This mechanism involves one of the fatty acid chains of a lipid flipping out of the bilayer and binding to the hydrophobic crevice of the protein (Tuominen et al., 2002). Association of other peripheral membrane-bound proteins

like protein myristoylated alanine-rich C-kinase substrate, K-Ras, and human carbonic anhydrase IV possibly also utilize this mechanism (Murray et al., 2002; Dell'Aqua et al., 1998; Faux and Scott, 1996). Accordingly, protein- and peptide-membrane interactions can be significantly reinforced through attachments of acyl chains to proteins/peptides that anchor these to the membrane surface. Additionally, Tyr and Trp residues, often found at the membrane-water interfaces, might also contribute to such anchoring (Meijer et al., 2001). Membrane anchoring has also been proposed to facilitate peptide translocation along the lipid membrane and consequently to increase the lifetime of the specific interaction between the anchored peptide and its target receptor. This mechanism might contribute to the increased response of the insulin receptor as observed when subjected to acylated insulin (Kurtzhals et al., 1996; Markussen et al., 1996).

Interaction of membrane-anchored peptides with lipid membranes will depend on the physicochemical properties of the membrane that are influenced by, for instance, temperature, the nature of the membrane headgroups, and the chemical composition of the acyl chains of the membrane. Knowledge of the molecular basis of these peptide-lipid interactions is not only essential for designing antimicrobial peptides but might also be exploited in designing drug delivery systems based on acylated peptides (Pedersen et al., 2001a,b).

In contrast to studies of antimicrobial peptides, only a few theoretical studies have been carried out to elucidate the interaction between peripheral peptides and their interactions with lipid membranes (La Rocca et al., 1999). This is, in part, because the structure of many peripheral peptides is not known. In the present study, we have used molecular dynamics (MD) simulations to investigate how a synthetic, cationic C_{14}-N-acylated peptide of sequence myristoyl-HWAHPGGHHA-amide (hereafter referred to as C_{14}-peptide) affects the structural and mechanical properties of dipalmitoylphosphatidylcholine (DPPC) lipid membranes in the fluid (L_{α}) state.

Structural characteristics of a membrane-associated peptide are not trivially obtained since the solution structure is not necessarily preserved when the peptide is brought into contact with a lipid bilayer (Gesell et al., 1997; Aliste et al., 2003). Therefore it is of importance to characterize both solution- and membrane-associated structures of these peptides. The only structural information of the C_{14}-peptide investigated in the present study is available from Fourier-transform infrared (FTIR) measurements suggesting that the membrane-associated C_{14}-peptide contains a β-sheet induced by a Pro residue centrally located in the sequence (Pedersen et al., 2001a,b). Since the solution as well as the membrane-associated structure of the C_{14}-peptide is unknown in atomic detail, we here deduce the fold of the C_{14}-peptide in an aqueous solution using MD simulations. Multiple simulations, carried out for several nanoseconds (ns) using different starting structures, were performed. The final structures were found to be very similar to each other, and one of them was chosen to further investigate the dynamics of the acylated form of the peptide and its influence on the properties of DPPC bilayers. Additionally we characterize changes in the solution structure of the peptide upon its association with the lipid membrane.

METHODS

In the following we describe first the modeling approach used to obtain the peptide structure. We then outline the procedure for constructing the combined C_{14}-peptide-DPPC system, and finally we rationalize our choice of statistical ensembles used in the membrane simulations.

Peptide modeling

The peptide sequence HWAHPGGHHA was assembled using the Swiss PDB-viewer (http://www.expasy.org/spdbv). The sequence was heated to 1000 K over a short 5-ps simulation in vacuum. To obtain six independent starting conformations of the peptide, this procedure was repeated six times while assigning random initial velocities. The six peptide conformations were subsequently solvated in a rectangular box with equilibrated SPC water molecules (Berendsen et al., 1987). Initial dimensions were 40.3 × 40.5 × 35.9 Å^3. The distance between the periodic images of the peptide was initially 26 Å, 26 Å, and 21 Å along the x-, y-, and z-directions, respectively. The total system size was $N = \sim6000$ atoms.

To deploy a relatively large 5-fs time step and thereby the ability to reach relatively long (50-ns) simulation times, we eliminated all high frequency bond vibrational modes using the GROMOS96 united atom force field (van Gunsteren and Berendsen, 1987, 1996) with the polar hydrogen atoms constrained through dummy atom constructs. The MD program GROMACS (Berendsen et al., 1995; Lindahl et al., 2001) was applied together with the LINCS algorithm that constrains all bond-lengths with high computational efficiency (Hess et al., 1997; Lindahl et al., 2001). Five of the six systems were simulated for 50 ns at 298 K at constant temperature T and volume V (NVT ensemble) using a cutoff of 10 Å for computation of all nonbonded interactions. Full periodic boundary conditions were applied. As a check of the sensitivity of the obtained peptide structure(s) to the method by which the electrostatic forces were computed, we carried out the simulation of the sixth system using the particle mesh Ewald method (PME) for the computation of the electrostatic forces (Darden et al., 1993; Essmann et al., 1995). A grid spacing of 1.2 Å was applied, and a fourth-order spline was used for interpolation. The remaining part of the simulation protocol was left invariant. As seen from Fig. 1, six very similar peptide configurations were obtained after 6 × 50 ns of NVT simulation. No significant structural difference could be ascribed to the two different ways the electrostatic forces were calculated; the structure obtained using the PME method displays a backbone fold very similar to that of the five other conformations. One configuration (configuration 2) was arbitrarily chosen for further studies, where the N-terminal was acylated and anchored to a DPPC membrane as outlined in the following.

DPPC$^+$ modeling

The initial configuration of 72 DPPC lipid molecules and 2092 water molecules corresponding to a hydration of 29 water molecules per lipid was taken from earlier published work (Feller et al., 1997a; Feller and Pastor, 1999). In the following, we denote this system $DPPC^-$, i.e., a DPPC bilayer without peptide. Similarly, $DPPC^+$ refers to a DPPC membrane with the anchored peptide, and $DPPC^{\pm}$ to both. In constructing DPPC$^+$ (see Fig. 2), the peptide was initially placed on top of the DPPC membrane with the DPPC/water coordinates rescaled to yield x,y,z-dimensions of 47.6 × 47.6
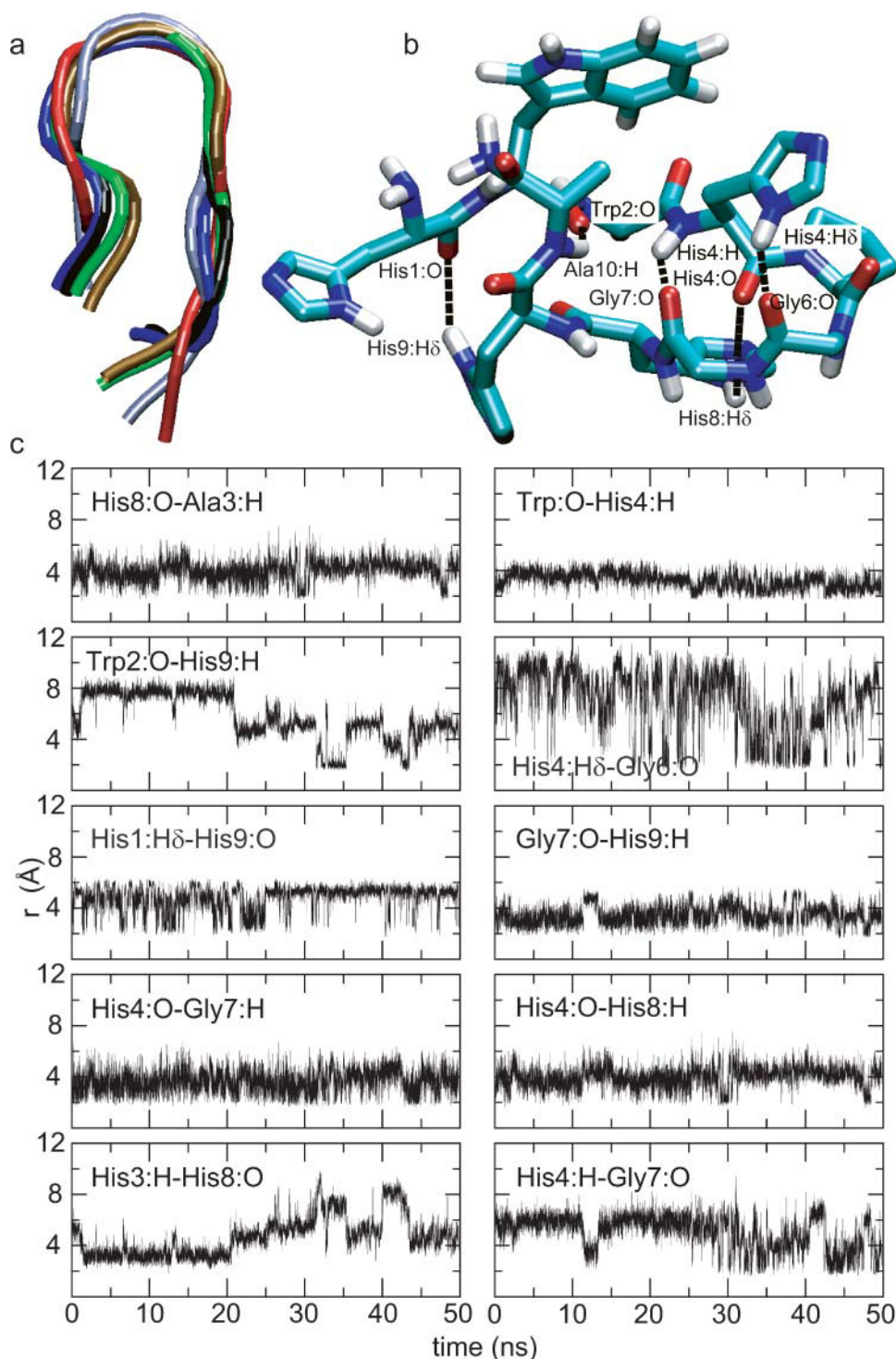
FIGURE 1 (*a*) Superposition of the six final configurations of the HWAHPGGHHA-peptide obtained after 6×50 ns of *NVT* simulation at $T = 298$ K. Configuration 6, shown in black, is obtained from a simulation in which the PME method was used for computation of the electrostatic forces (see text for more details). The root mean-square deviation (RMSD, all backbone atoms included) between configuration 2 (arbitrarily chosen as reference) and configurations 1, 3, 4, 5, and 6 are 2.1 Å, 1.8 Å, 2.0 Å, 1.5 Å, and 2.2 Å, respectively. (*b*) Hydrogen bonding pattern in a representative peptide configuration obtained after 50 ns of MD simulation. The following hydrogen bonds are shown: His^1:O-His^9:H_δ, Ala^{10}:H-Trp^2:O, His^4:H-Gly^7:O, His^8:H_δ-His^4:O, and His^4:H_δ-Gly^6:O. (*c*) Time-evolution of selected hydrogen bonds monitored over 50 ns of the peptide simulation in water (*configuration 2*). Bond lengths between hydrogen acceptors and donors below 3.5 Å are considered to indicate hydrogen bonds.

$\times$ 66.9 Å^3, which satisfies the experimental area per DPPC molecule of 62.9 Å^2 (Nagle et al., 1996). One lipid molecule in the bilayer center was subsequently modified as follows: The headgroup and one acyl chain were removed. The retained palmitoyl (C$_{16}$) acyl chain was modified to a myristoyl (C$_{14}$) chain by removing the terminal methyl group, the two hydrogen atoms of the methylene group next to the methyl group, and converting the carbon atom of the methylene group into a hydrogen atom. The carbonyl carbon atom of the resulting C$_{14}$ chain was joined to the peptide through an amide linkage. The position of the resulting C$_{14}$-peptide and the angle of the backbone relative to the surface of the membrane were adjusted such that the side chain of Trp^2 was located in the carbonyl (headgroup) region. To ensure that the C$_{14}$-peptide had no major clashes with the neighboring lipids, a few lipids near the C$_{14}$-peptide were rearranged by translation in the membrane (*x–y*)-plane. The resulting distances between the periodic images of the C$_{14}$-peptide were initially 34 Å, 34 Å, and 40 Å along the *x*-, *y*-, and *z*-directions, respectively. Similar to the
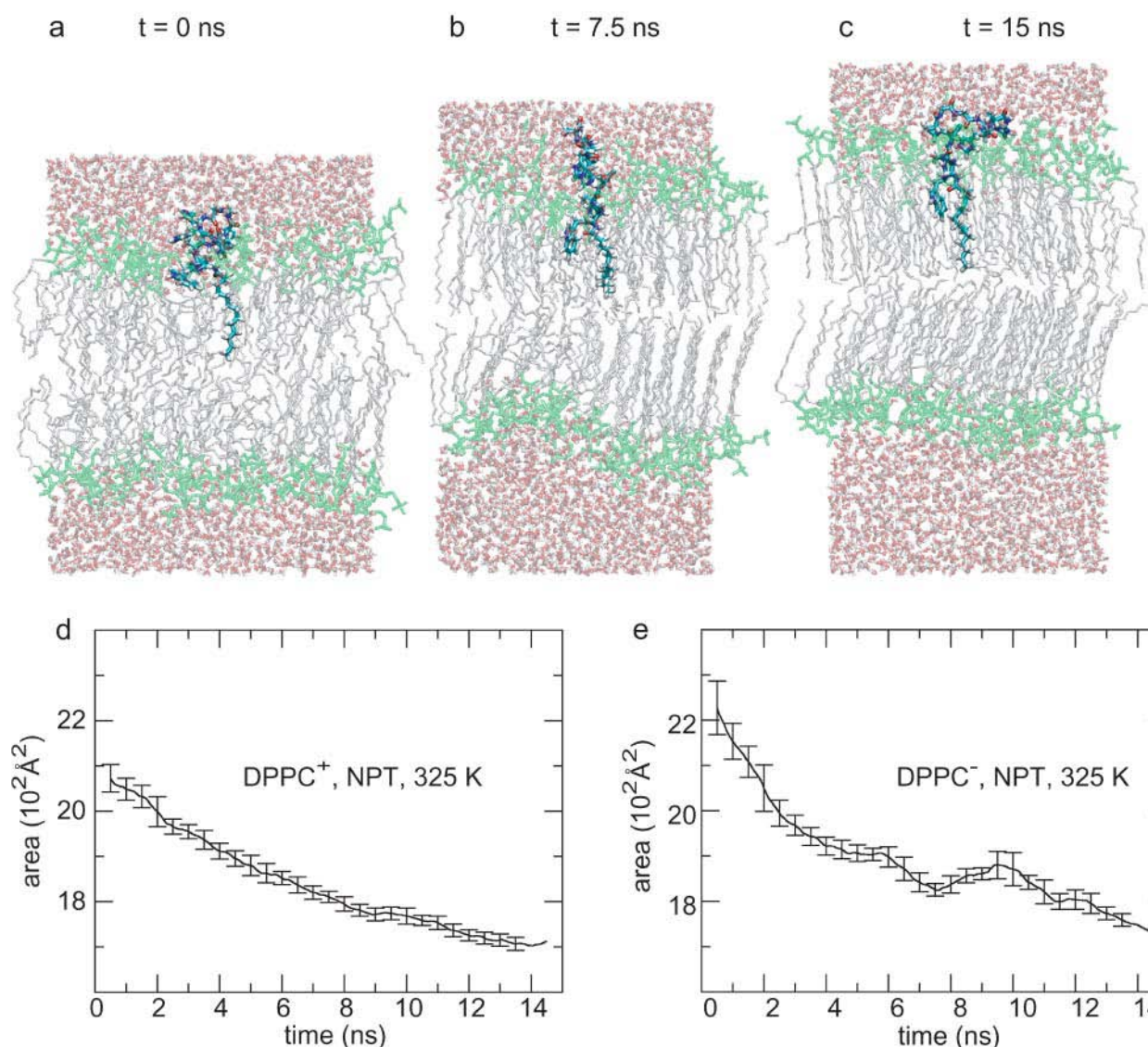
FIGURE 2 Snapshots of the combined system (DPPC$^+$) simulated in the *NPT* ensemble at 0 ns (*a*), 7.5 ns (*b*), and 15 ns (*c*) of the MD simulation at 325 K. The C$_{14}$-peptide is shown in licorice and with conventional color coding. Water molecules are shown in red (*O*) and white (*H*). The choline headgroup and acyl chains of the DPPC membrane are shown in green and gray, respectively. Ordering and tilt of the lipid acyl chains are seen to increase with simulation time as is the overall bilayer thickness (see text for further discussion). Corresponding DPPC$^+$ areas as a function of time are shown in *d*. For comparison, total areas of DPPC$^-$ obtained within the *NPT* ensemble are displayed in *e*. The error bars in the areas in *d* and *e* depicts area fluctuations as 1-ns running averages.

C$_{14}$-peptide in the experiment (Pedersen et al., 2001a,b), the C-terminal of the C$_{14}$-peptide was amidated. Furthermore, the experiments suggest that the C$_{14}$-peptide is divalent and cationic (Pedersen et al., 2001a,b). Therefore we protonated residues His^8 and His^9 since these residues were located nearest to the aqueous phase. However, as discussed below protonation states of any His residue of the C$_{14}$-peptide cannot be consistently determined. Two water molecules were replaced by two chloride anions to obtain a neutral total system.

Simulation of DPPC$^\pm$ in the *NPT* ensemble

The CHARMM27 parameter set (MacKerell et al., 1998; Feller and MacKerell, 2000) was used with the TIP3 water model (Jorgensen et al., 1983) for the simulations of DPPC$^+$. All parameters needed to represent the C$_{14}$-peptide were available from this parameter set. The simulations were

carried out using NAMD (Kalé et al., 1999). The most natural choice of an ensemble in membrane simulations and in particular when studying peptide anchoring is the *NPT* ensemble since the lateral area of DPPC$^+$ is unknown (Zhang et al., 1995). Hence, this ensemble was our initial choice.

A time step of 1 fs was used in all simulations. A constant ambient pressure of $P = 1$ atm was imposed using the Langevin piston method of Feller et al. (1995) with a damping coefficient of 5 ps^{-1} and a piston period of 100 fs. The PME method was used for computation of the electrostatic forces (Darden et al., 1993; Essmann et al., 1995). The grid spacing was kept below 1.0 Å, and a fourth-order spline was used for the interpolation. The long-range part of the electrostatic forces was evaluated every fourth fs. The van der Waals interactions were cut off at 12 Å using a switching function starting at 10 Å. Periodic boundary conditions were imposed in all directions.

Firstly, the DPPC$^\pm$ systems were energy-minimized. For DPPC$^+$, the minimization was followed by 100 ps of equilibration at constant

temperature T and pressure P (*NPT* ensemble) with $T = 325$ K and $P = 1$ atm. The C_{14}-peptide but not its anchor was kept fixed in this early equilibration phase. Subsequently the C_{14}-peptide was released, the full (unconstrained) system was energy-minimized, and simulations were performed for 15 ns in the *NPT* ensemble with $T = 325$ K and $T = 350$ K.

Similarly, simulations of DPPC$^-$ were performed for 15 ns in the *NPT* ensemble at $T = 325$ K and $T = 350$ K with starting coordinates taken from the original DPPC$^-$ system (Feller et al., 1997a; Feller and Pastor, 1999) rescaled to yield an initial area per DPPC molecule of 62.9 Å. Although different experimental areas have been reported (see for instance, Lemmich et al., 1996), 62.9 Å is the experimental value (Nagle et al., 1996), most frequently used in stringently testing simulations of DPPC bilayers against experimental data (Feller et al., 1997a; Feller and Pastor, 1999; Feller and MacKerell, 2000; Lindahl and Edholm, 2000; Åman et al., 2003).

Properties of DPPC$^\pm$ in the *NPT* ensemble

From the *NPT* trajectories of DPPC$^\pm$ we calculated the area per lipid molecule. As demonstrated in Fig. 2, *d* and *e*, the *NPT* simulations at 325 K do not result in a reasonable equilibrium area for the fluid phase of DPPC$^\pm$ (similar results were observed for 350K; data not shown). The final value for the projected area in DPPC$^-$ at $t = 15$ ns is ~1750 Å^2 or 48.6 ± 2.5 Å^2 per molecule and is significantly smaller than the experimental value of 62.9 Å^2. Furthermore, the membrane in Fig. 2 exhibits substantial structural ordering of the acyl chains after 15 ns (the same holds for the DPPC$^-$ system). Order parameter profiles (data not shown) indicate that a liquid-to-gel phase transition occurs on the 15-ns timescale giving rise to a large lipid ordering. Similar trends have been observed in short 1-ns simulations of DPPC membranes (Feller and Pastor, 1999) under constant ambient pressure and temperature using the CHARMM22 force field (Schlenkrich et al., 1996; Feller et al., 1997b). After 1 ns, the nonconverged membrane area obtained was ~5% smaller than the experimental value and the lipid order parameter profiles were consequently higher than the experimental data (Feller and Pastor, 1999). These results led to a reparameterization of the CHARMM22 force field producing the CHARMM27 parameters (Feller and MacKerell, 2000) as deployed here. However, as demonstrated by our results this reparameterized parameter set does not improve the value for the area per molecule in the *NPT* ensemble (Fig. 2). In fact, the incorrect area is hidden in the parameterization which was carried out in the *NP$_z$AT* ensemble (MacKerell et al., 1998; Feller and MacKerell, 2000). In contrast, a decrease in lipid area per molecule with simulation time during *NPT* simulations of small-sized DPPC patches was not seen in recent 100-ns *NPT* simulations of 64 united atom DPPC molecules with 23 waters per lipid. Optimized potentials for liquid simulations-based van der Waals parameters (Berger et al., 1997) were deployed (Åman et al., 2003) and despite the small system size, the average area per molecule was ~63 Å^2 (Åman et al., 2003) in agreement with experimental data (Nagle et al., 1996). Therefore it is not obvious that one should resort to application of surface tensions when simulating small membrane patches as suggested earlier (Feller and Pastor, 1999; Feller and MacKerell, 2000). The issue of surface tensions in bilayer simulations was critically examined in Marrink and Mark (2001). The authors found that undulatory motions clearly are suppressed in bilayers simulated at different constant areas leading to nonzero surface tensions reaching up to 100 dyn/cm. Consequently, one expects that in bilayers subjected to applied stress, i.e., tension, computed compressibility moduli could be biased by the tension. Furthermore, the tension that one must apply to obtain a correct area per molecule is inversely proportional to the size of the membrane patch simulated (Lindahl and Edholm, 2000). Nevertheless, besides reparameterization (Feller and MacKerell, 2000), constant surface tension simulations, well documented in the literature (Tieleman and Berendsen, 1996; Feller et al., 1997a; Feller and Pastor, 1999; Feller and MacKerell, 2000), seem to be the only reliable approach to obtain correct areas per molecules when using the improved CHARMM27 parameter set for lipids in simulations of small membrane patches. Therefore we resort to constant area (A) and constant surface tension (γ) simulations through

applications of the *NP$_z$AT* and *NP$_z\gamma T$* ensembles, respectively, to gauge the influence on bilayer mechanical properties when anchoring a peptide to fluid DPPC membranes.

Simulations of DPPC$^\pm$ in the *NP$_z$AT* and *NP$_z\gamma T$* ensembles

We specified the range of applied tensions by performing an initial constant area, constant normal pressure (P_z) simulation (*NP$_z$AT* ensemble) of DPPC$^-$ for 2 ns. The area $A = 62.9$ Å^2 corresponds to the experimental area per molecule. A constant normal pressure P_z of 1 atm normal to the bilayer (z-direction) and a temperature $T = 325$ K was ensured using the Langevin piston method (Feller et al., 1995; Zhang et al., 1995). The remaining part of the simulation parameters were kept as in the *NPT* simulations.

From the *NP$_z$AT* simulation we calculated the average surface tension $\bar\gamma$ (conjugate to A) as the time average of the pressure tensor (Zhang et al., 1995; Feller et al., 1997a),

$$\bar{\gamma} = \langle L_z(t)\{P_{zz}(t) - 1/2[P_{xx}(t) + P_{yy}(t)]\}\rangle_t. \quad (1)$$

We, as others (Feller and Pastor, 1999; Tieleman and Berendsen, 1996), conducted subsequently constant surface tension simulations while imposing a range of surface tensions around the average surface tension $\bar\gamma = 40.6 \pm 15.8$ dyn/cm as calculated from the *NP$_z$AT* simulation of DPPC$^-$ with $A = 62.9$ Å^2 at 325 K (see also Results and Discussion and Table 1). Given the computed average value $\bar\gamma$ and its fluctuation σ^γ we decided to conduct *NP$_z\gamma T$* simulations, each for 14 ns, with applied surface tensions of $\gamma = 35, 41, 46, 51$ 56, 61, and 70 dyn/cm of DPPC$^\pm$ at $T = 325$ K (see Table 1). The series of constant surface tension simulations allows us to examine the influence of the peptide on the bilayer area compressibility modulus K_A (from Allen and Tildesley, 1988):

$$\left(\frac{\partial\gamma}{\partial A}\right)_T = \frac{K_A}{A_0} \quad (2)$$

$$\sigma_A^2 = k_B T \left(\frac{\partial A}{\partial\gamma}\right)_T = k_B T \frac{A_0}{K_A}, \quad (3)$$

where γ is the applied surface tension, A_0 is the total (experimental) membrane area at the free energy minimum, i.e., $(\partial G/\partial A)_{T,A=A_0} = 0$, k_B is the Boltzmann constant, and T is the absolute temperature. From Eq. 2 we intend to quantify to which extent the anchored peptide affects K_A, a key mechanical property of lipid membranes.

Protonation states of histidine residues

The peptide studied contains four titratable residues His[1], His[4], His[8], and His[9]. Partly due to the lack of the three-dimensional structure of the peptide we cannot consistently assign protonation states before the simulations. In the peptide-water simulations we choose all His as neutral (see above). As discussed, all six simulations resulted in a β-sheet conformation of the peptide as also suggested by FTIR measurements. It therefore appears that our initial choice of the protonation state was reasonable. To further validate this point, we estimated pK_a values of the His residues using selected frames of the peptide-water simulation.

The pK_a values of the His residues were estimated using the so-called single site titration model (Bashford and Karplus, 1990; Antosiewicz et al., 1994). Briefly, one evaluates the potential field at each titratable group by solving the Poisson-Boltzmann equation using the UHBD program (Madura et al., 1995; Davis and McCammon, 1991). The electrostatic potentials are deployed to estimate apparent pK_a values using the *Hybrid* procedure

TABLE 1 Summary of simulations

System	Ensemble	A (Å²)	A' (Å²)	$\bar{A} \pm \sigma^{\bar{A}}$ (Å²)	$\bar{A}' \pm \sigma^{\bar{A}'}$ (Å²)	γ (dyn/cm)	$\bar{\gamma} \pm \sigma^{\bar{\gamma}}$ (dyn/cm)
DPPC⁻	NP_zAT	2265.8	62.9	—	—	—	40.6 ± 15.8
DPPC⁻	$NP_z\gamma T$	—	—	1814.7 ± 26.3	50.4 ± 0.7	35	—
DPPC⁻	$NP_z\gamma T$	—	—	1858.7 ± 22.5	51.6 ± 0.6	41	—
DPPC⁻	$NP_z\gamma T$	—	—	1869.1 ± 26.5	51.9 ± 0.7	46	—
DPPC⁻	$NP_z\gamma T$	—	—	2219.3 ± 62.4	61.7 ± 1.7	51	—
DPPC⁻	$NP_z\gamma T$	—	—	2051.7 ± 51.6	57.0 ± 1.4	56	—
DPPC⁻	$NP_z\gamma T$	—	—	2238.1 ± 52.2	62.2 ± 1.5	61	—
DPPC⁺	$NP_z\gamma T$	—	—	2020.5 ± 17.4	—	35	—
DPPC⁺	$NP_z\gamma T$	—	—	2017.7 ± 50.0	—	41	—
DPPC⁺	$NP_z\gamma T$	—	—	2148.9 ± 31.1	—	46	—
DPPC⁺	$NP_z\gamma T$	—	—	2006.3 ± 33.4	—	51	—
DPPC⁺	$NP_z\gamma T$	—	—	2205.6 ± 72.5	—	56	—
DPPC⁺	$NP_z\gamma T$	—	—	2741.9 ± 59.5	—	61	—
DPPC⁺	$NP_z\gamma T$	—	—	3086.3 ± 94.6	—	70	—

DPPC$^\pm$ refers to pure($-$) and C$_{14}$-peptide-containing ($+$)DPPC membranes, respectively; NP_zAT and $NP_z\gamma T$ refer to simulations with constant area A and constant applied surface tension γ in the range 35–70 dyn/cm, respectively. In both ensembles, a constant normal pressure (P_z) of 1 atm is imposed. Key: $\bar{\gamma}, \sigma^{\bar{\gamma}}$ denotes average surface tension and its root mean-square fluctuation calculated from the last nanosecond of the NP_zAT trajectory of DPPC$^-$; $\bar{A}, \sigma^{\bar{A}}$ refers to average projected area and root mean-square fluctuations for the complete membrane; and $\bar{A}', \sigma^{\bar{A}'}$ refers to the similar quantities per lipid for DPPC$^-$ only. Areas and area fluctuations were calculated from the last 4 ns of the $NP_z\gamma T$ trajectories for both DPPC$^-$ and DPPC$^+$ using here 10 windows of a width of 0.4 ns to compute 10 individual average areas. The total average area listed and its fluctuations were obtained from the individual areas. The value $\gamma = 70$ dyn/cm is omitted for DPPC$^-$, since $\gamma = 61$ dyn/cm reproduced the experimental area per molecule in DPPC$^-$. Hence, we mainly focus on DPPC$^+$ with $\gamma = 61$ dyn/cm when addressing effects resulting from membrane-anchoring a peptide.

(Gilson, 1993). The atoms of the peptide were assigned point charges from the CHARMM27 force field. The dielectric constant of the solvent was $\epsilon = 80$ and the dielectric constant of the molecular interior was set to $\epsilon = 20$ (Antosiewicz et al., 1994) in the calculation using peptide conformations extracted from the peptide simulations in water. The ionic strength was 0.15 M (physiological conditions). Further details are provided in Davis et al. (1991) and Peters et al. (1999).

The results from the peptide-water trajectories indicate that the pK$_a$ value of His varies between ~5 and 6.5, which, as observed in other systems, is mainly caused by peptide flexibility (You and Bashford, 1995; Beroza and Case, 1996; Alexov and Gunner, 1997). There is currently no consistent approach that allows adjustment of charges during simulations and at the same time conserving appropriate thermodynamic statistics within the adopted ensemble. Moreover, the pK$_a$ calculations are based on a continuum model and, as discussed in the literature, have their limitations (Gorfe et al., 2002). For instance, this model cannot accurately account for the existence of tautomeric states arising from the uncertainty in the location of the protons on the imidazole ring.

In the DPPC$^+$ simulations protonation states are more difficult to determine. Initially, we protonated His[8] and His[9], since experiments conducted at pH 7 indicate two charged His residues (but not which ones). We performed pK$_a$ calculations for DPPC$^+$ to inspect this assignment treating water phase and membrane environment as a continuum medium by varying in this case the dielectric constant between 20 (lipid phase) and 80 (aqueous phase). The resulting pK$_a$ values, indicating that His could possibly be partially charged (depending on C$_{14}$-peptide conformation), are much less reliable than the corresponding pK$_a$ values obtained for the peptide-water system, since the macroscopic approach neglects peptide-lipid headgroup interactions. Inspection and quantification of our DPPC$^+$ trajectories reveal that these interactions consistently occur throughout our simulations of the interfacially bound C$_{14}$-peptide. Consequently, a more reliable estimate would require a microscopic (noncontinuum) approach (Sham et al., 1997) and protonation state of His[8] and His[9] can neither be confirmed nor contradicted.

RESULTS AND DISCUSSION

In the following we first present and discuss the results of the MD simulations of the peptide in aqueous solution. This

section is followed by Results and Discussion of our simulations of DPPC$^\pm$.

Peptide properties in aqueous solution

The folding of the peptide was carried out at constant volume since the peptide-water systems initially constructed were not expected to undergo substantial density changes during the simulations. In accord with this assumption, we found average pressures in all peptide-water system in the range ~-100 ± 260 bar to ~20 ± 260 bar. The six peptide-water trajectories exhibit an average pressure of -43 ± 39 bar. Hence, no artificial pressures biasing the conformational sampling were present in any of the systems.

The convergence of the peptide fold was examined by following the time evolution of thermodynamic and structural quantities of the peptide during the 6×50 ns NVT simulation. Peptide total (free) energy, root mean-square deviation (RMSD) of the peptide relative to the initial structure, the number of hydrogen bonds, and the solvent-exposed surface area as well as the overall secondary structure were monitored.

In all six simulations a β-sheet, induced and stabilized by Pro[5] in the β-bend (loop) region, was formed (Fig. 1 a). One representative hydrogen bonding pattern stabilizing the β-sheet conformation is shown in Fig. 1 b for configuration 2 obtained after 50 ns. The β-sheet structure observed in the simulations is in accord with FTIR measurements probing secondary structure and suggesting, for this peptide, a β-sheet structure (Pedersen et al., 2001a,b). Backbone kinks induced by Pro residues can lead to characteristic motions of the nearby region

(Tieleman et al., 1999). Such motions will lead to breakage and (re-)formation of the hydrogen bonds between, for instance, the backbone atoms. The persistence time of some individual hydrogen bonds formed in configuration 2 is shown in Fig. 1 *c*. The total number of peptide-peptide hydrogen bonds is 5 ± 1. The number of peptide-water hydrogen bonds is also constant in time; 22 ± 3. Therefore the water-exposed fraction of the peptide and thus its conformation, remains constant in accord with solvent-accessible surface area calculations (see data in Supplementary Material). Breakage and (re-)formation of several of the hydrogen bonds formed between the donor-acceptor atoms occur (Fig. 1 *c*). Two to three of these are between the backbone atoms. This fluctuating hydrogen bonding pattern over time partly reflects (ϕ, ψ) rotations around the peptide backbone as the backbone explores the conformational space (data not shown).

The secondary structure map of the peptide computed as a function of simulation time using DSSP (Kabsch and Sander, 1983) is illustrated in Fig. 3 *a* (configurations 2 and 6; electrostatic forces computed with a 10 Å cutoff and with the PME method, respectively; see Methods). The structure maps confirm that a β-bend region (*green*) consistently is featured around Pro[5]. At times this region also classifies as a β-turn region (*yellow*); i.e., the backbone curvature is either above (bend) or below (turn) 70° (Kabsch and Sander, 1983). This suggests C- and N-terminal peptide flexibility such that end-to-end distance may vary. The region around Pro[5] forms occasionally a β-bridge (*black*) through intramolecular hydrogen bonding. Most frequently this occurs for configuration 2. Even more rarely a β-sheet conformation is featured by configuration 2, although this never happens for configuration 6. Hence, the alternating hydrogen bonding pattern observed along the trajectories (compare to Fig. 1 *c*) is indicative of, and consistent with, small changes in secondary structure over time resulting in either a β-bend, a β-turn, a β-bridge, or a β-sheet region (Fig. 3 *a*). These structural characteristics (or transitions) are manifested by peptide backbone rotations along with hinge-like motion around Pro[5].

C$_{14}$-peptide structural properties in DPPC^{+}

In this section we analyze the overall structure and corresponding structural fluctuations of the C$_{14}$-peptide in DPPC^{+}.

Secondary structure

We computed the secondary structure of the C$_{14}$-peptide as a function of simulation time for all surface tensions applied. Results are shown in Fig. 3 *b* while omitting the results for $\gamma = 70\,\text{dyn/cm}$ where the secondary structure mainly classifies as coil. The structure maps shown in Fig. 3 *b* are perhaps the most transparent comparison with the corresponding
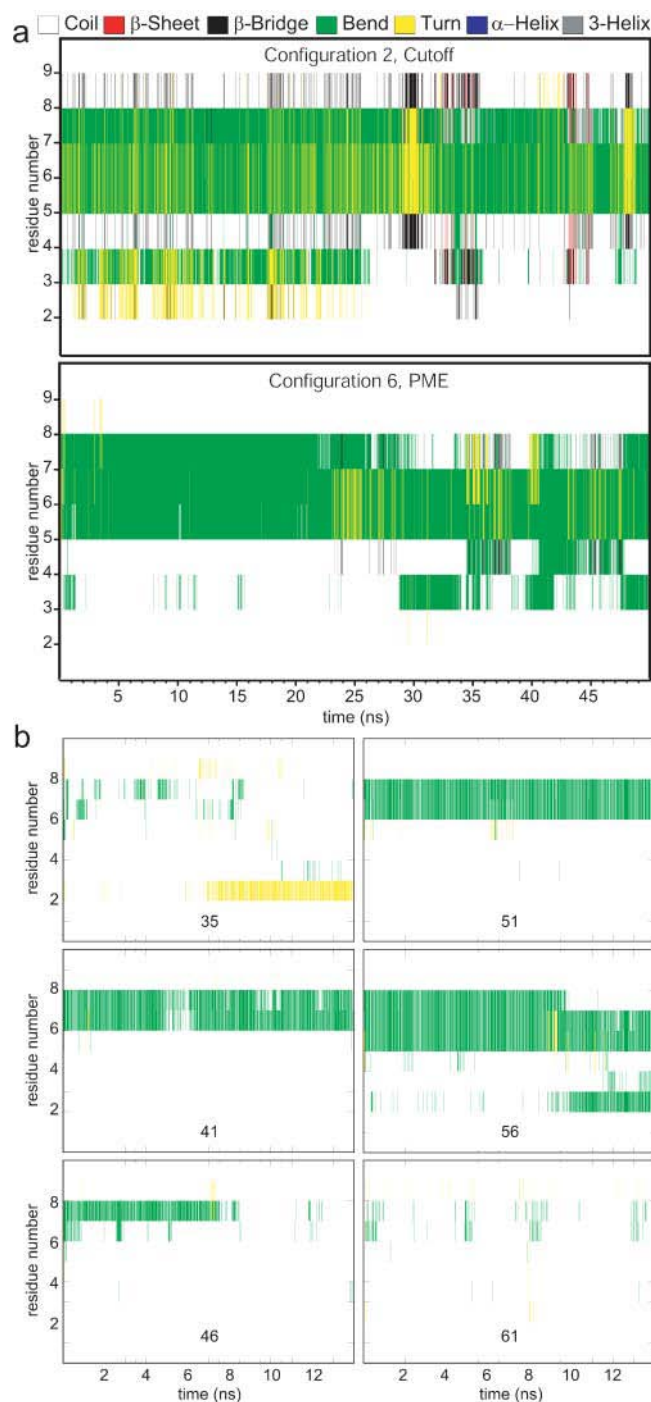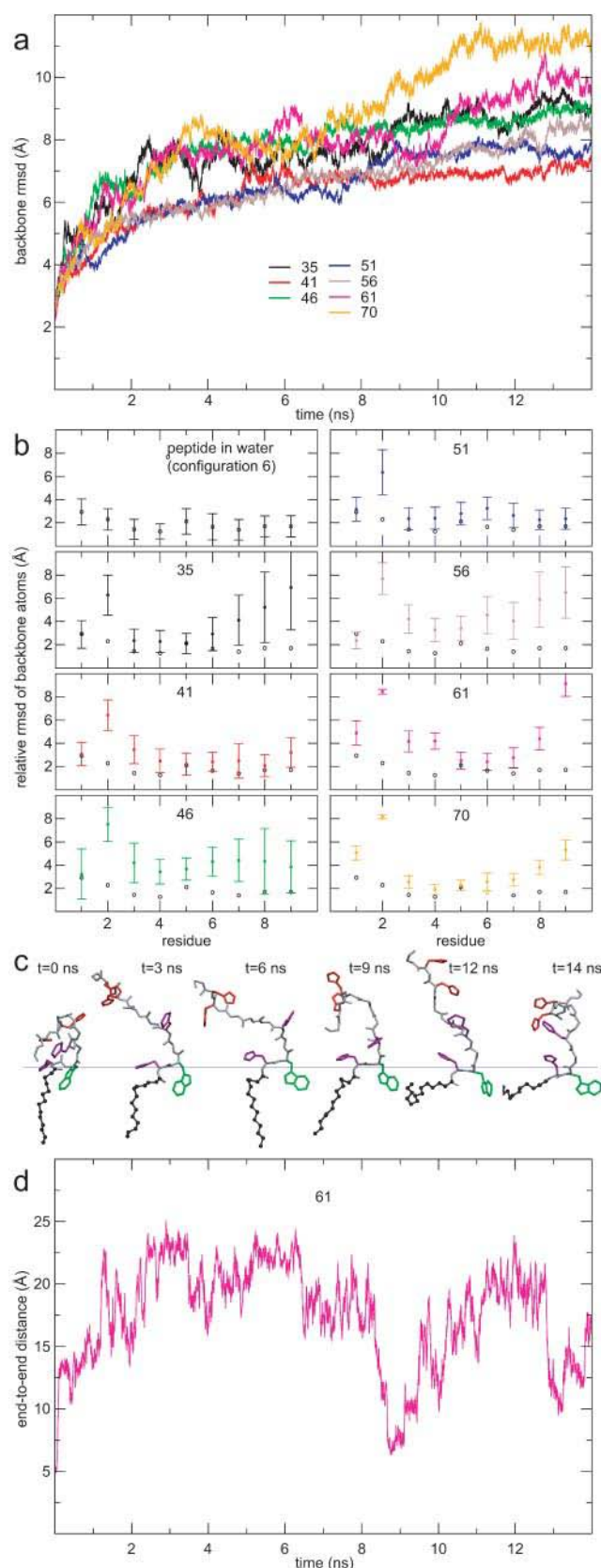

FIGURE 3 (*a*) Peptide secondary structure per residue along the trajectories of peptide configurations 2 and 6. The secondary structure was computed with the program DSSP (Kabsch and Sander, 1983). The inset lists the color coding that classifies the computed secondary structure. For configurations 2 and 6, electrostatic forces were computed with a 10 Å cutoff and with the PME method (Darden et al., 1993), respectively (see text for details). (*b*) Peptide secondary structure for DPPC^{+} from simulations performed with $\gamma = 35$, 41, 46, 51, 56, and 61 dyn/cm as given in the inset. For $\gamma = 70$ dyn/cm, the C$_{14}$-peptide features predominantly coil as secondary structure and its structure map is therefore omitted.

FIGURE 4 (*a*) Root mean-square deviation (*RMSD*) of the C$_{14}$-peptide backbone in DPPC$^+$ as a function of simulation time. Applied surface tensions are given in the inset. The RMSD was calculated relative to the $t = 0$ structure. (*b*) Residue-residue RMSD of the C$_{14}$-peptide in water and in DPPC$^+$. The RMSD values for the peptide in water were obtained after aligning all backbone atoms (C, O, C$_\alpha$, N) to the final $t = 50$ ns structure and were averaged over the last 25 ns of the simulation. The data shown represent configuration 6 in which the PME method was used for computation of the electrostatic forces (see text for more details). RMSD values for configurations 1–5 are similar (data not shown). In DPPC$^+$, RMSD values were obtained after aligning all backbone atoms (C, O, C$_\alpha$, N) to the $t = 14$ ns structure. The RMSD values are averaged over the last 4 ns of the DPPC$^+$ simulations. (*c*) Conformational transitions of the C$_{14}$-peptide in DPPC$^+$ with $\gamma = 61$ dyn/cm. Representative C$_{14}$-peptide snapshots were taken at $t = 0, 3, 6, 9, 12,$ and 14 ns. The C$_{14}$-peptide backbone and the acyl anchor is shown in gray and black, respectively. Protonated (His[8] and His[9]) and neutral (His[1]) His residues are shown in red and purple, respectively, and Trp[2] is shown in green. The horizontal blue line is a guide to the eye to delineate an approximate location of the lipid membrane. Large changes in the C$_{14}$-peptide end-to-end distance (r_{ee}, defined as the distance between the C$_\alpha$ atoms of residues 1 and 10) of the C$_{14}$-peptide accompany the conformational transitions in *c* as demonstrated in *d*, where r_{ee} is displayed as a function of time for DPPC$^+$ with $\gamma = 61$ dyn/cm.

(secondary) structure of the water-solubilized peptide in Fig. 3 *a*. No systematic variation in secondary structure with γ is featured. We find for the C$_{14}$-peptide that a β-bend region (*green*) in the middle of the C$_{14}$-peptide is most frequently occurring and is therefore the most well-preserved secondary structural element in simulations at different γ. This preservation also holds relative to the water-solubilized peptide (Fig. 3 *a*). The middle region of the C$_{14}$-peptide occasionally classifies as a β-turn region (*yellow*) as also seen for the water-solubilized peptide (Kabsch and Sander, 1983; backbone curvature either above (bend) or below (turn) 70°). We find for the $\gamma = 35$ dyn/cm simulation that the secondary structure of the C$_{14}$-peptide differs the most relative to the structures of the other C$_{14}$-peptides in Fig. 3 *b* and relative to the corresponding structures in water (Fig. 3 *a*). In this simulation a β-turn is at times present at residues 2–3 and 8–9, i.e., toward the termini, reflecting that the mode of interaction with the lipid bilayer could be different at lower applied tension where the bilayer in fact is too compact. However, at $\gamma = 61$ dyn/cm where the bilayer is laterally more expanded and its area corresponds to the experimental value (in DPPC$^-$ as discussed below), the secondary structure differs in a related manner, reflecting that the C$_{14}$-peptide in general interacts with the lipid bilayer in a complex mode involving peptide conformational transitions.

C$_{14}$-peptide structural fluctuations

We further analyzed the C$_{14}$-peptide structure in DPPC$^+$ by computing the RMSD of the peptide backbone relative to the initial ($t = 0$ ns) structure as a function of time and per-residue RMSD backbone fluctuations (Fig. 4, *a* and *b*) for all

applied tensions. These two properties are measures of peptide structural changes occurring upon anchoring that are not necessarily borne out in the secondary structure maps in Fig. 3.

The RMSDs closely approach convergence or even converge at $t = 14$ ns in all our simulations. After 10 ns we observe that the drift in the RMSD is small (Fig. 4 *a*). Computed relative to the water-solubilized peptide structure ($t = 0$ ns), RMSD changes with time are nevertheless notable and arise from several contributions: 1), from confining the C-terminus, i.e., substantial conformational changes/transitions involving large movements of the N-terminus relative to the confined C-terminus occur; 2), from bringing the peptide from an aqueous solution into a lipid membrane environment; and 3), from protonating His[8] and His[9].

No systematic variation in RMSD with the applied surface tension is evident, presumably due to the fact that the majority of the C_{14}-peptide is mainly spatially translated at the different tensions. Differences in conformational changes by means of e.g., end-to-end distance r_{ee} (data not shown), reflect that at lower surface tensions ($\gamma = 35$–41 dyn/cm) the C_{14}-peptide cannot penetrate deeply into the laterally compact bilayer, which reduces peptide-membrane interactions. This implies that intraprotein electrostatic interactions are reinforced, which, however, do not necessarily lead to a more stable C_{14}-peptide structure. Such interactions might equally well lead to conformational changes as impaired by changes in RMSD with time (Fig. 4 *a*).

To examine structural fluctuations of the C_{14}-peptide in different regions of the peptide we calculated average RMSD and corresponding RMS-fluctuation residuewise for the C_{14}-peptide after first aligning the structures collected over the last 4 ns to the $t = 14$-ns structure. To compare with the corresponding quantities in the water-solubilized peptide we also carried out the same calculation for one representative configuration in this system. Here we aligned first the structures collected over the last 25 ns of the simulation to the $t = 50$ ns structure. The results are shown in Fig. 4 *b*. Although anchored we find that mobility of the C_{14}-peptide in DPPC$^+$ is rather extensive. The RMSD and RMS fluctuations are of similar magnitude as in water in the center of the peptide, but significantly increased, in general, toward the termini. Among the residues, Trp[2] exhibits the largest RMSD in DPPC$^+$ but not always a particularly large RMS-fluctuation, reflecting that Trp[2] locates in the lipid interface where the side-chain mobility is more confined. Anchoring to the bilayer also implies that the peptide RMSD, residuewise, increases the most toward the free C-terminus with the exception being the peptide in the $\gamma = 51$ dyn/cm simulation where the bilayer in fact is too compact. For $\gamma = 56$ or 61 dyn/cm, large C-terminal fluctuations can be recognized whereas the anchored, N-terminal part conformationally is more confined.

Conformational transitions

A peptide conformational transition occurring at the lipid interface is displayed in Fig. 4 *c* by means of snapshots at $t = 0, 3, 6, 9, 12$, and 14 ns in DPPC$^+$ with $\gamma = 61$ dyn/cm, which we, (again, discussed below), consider to be the appropriate DPPC$^+$ system given that the reference bilayer structure of DPPC$^-$ produced the experimental area per molecule with $\gamma = 61$ dyn/cm. The conformational transition of the peptide is seen to involve a large movement of the free C-terminus, reflected in substantial changes in peptide r_{ee} over time (Fig. 4 *d*). At times the peptide is extended (3, 6, and 12 ns) as well as folded (9 and 14 ns). Occasionally, stacking of His imidazole rings occur suggesting that stacking interactions might contribute in stabilizing the structure of the anchored peptide.

Dynamics of the C$_{14}$-peptide in DPPC$^+$

In this section we analyze peptide dynamics and peptide-bilayer collective modes in DPPC$^+$.

C$_{14}$-peptide trajectories

Fig. 5 *a* displays the center-of-mass trajectories of the C_{14}-peptide and of the acyl anchor over 14 ns. The trajectory color scale proceeds from red to blue with time. The C_{14}-peptide snapshots included are at $t = 7$ ns, i.e., in the middle of the trajectory corresponding to green-yellow color. We find that the C_{14}-peptide exhibits very dynamic behavior despite the anchor. The motion differs among the seven simulations with different γ. Differences in trajectories also reflect that the C_{14}-peptide only in part preserves conformation while anchored since conformational transitions affecting the center-of-mass position occur (Fig. 4).

A relatively large projected area (50–100 Å^2) of the membrane plane is sampled by the C_{14}-peptide motion. Motion along the membrane normal is pronounced albeit limited due to the energetic cost of exposing the acyl anchor to the aqueous phase and due to C_{14}-peptide-lipid headgroup electrostatic interactions. One expects that the entropic cost associated with stretching the anchor contributes to this energetic cost to a smaller extent. Qualitatively, the path traced out by the acyl anchor is of comparable magnitude to that traced out by the C_{14}-peptide, but overall the trajectories differ in shape and reveal that the anchor frequently curls up.

Concerted motions

To further examine the C_{14}-peptide-bilayer collective dynamics in DPPC$^+$ influenced by the acyl anchor we have analyzed the coupling of motion of the C_{14}-peptide along the membrane normal to that of the membrane. This coupling between the C_{14}-peptide (P) center-of-mass and the center-of-mass motion of the bilayer, resolved with radial distance r, from the C_{14}-peptide [$L(r)$] was quantified as
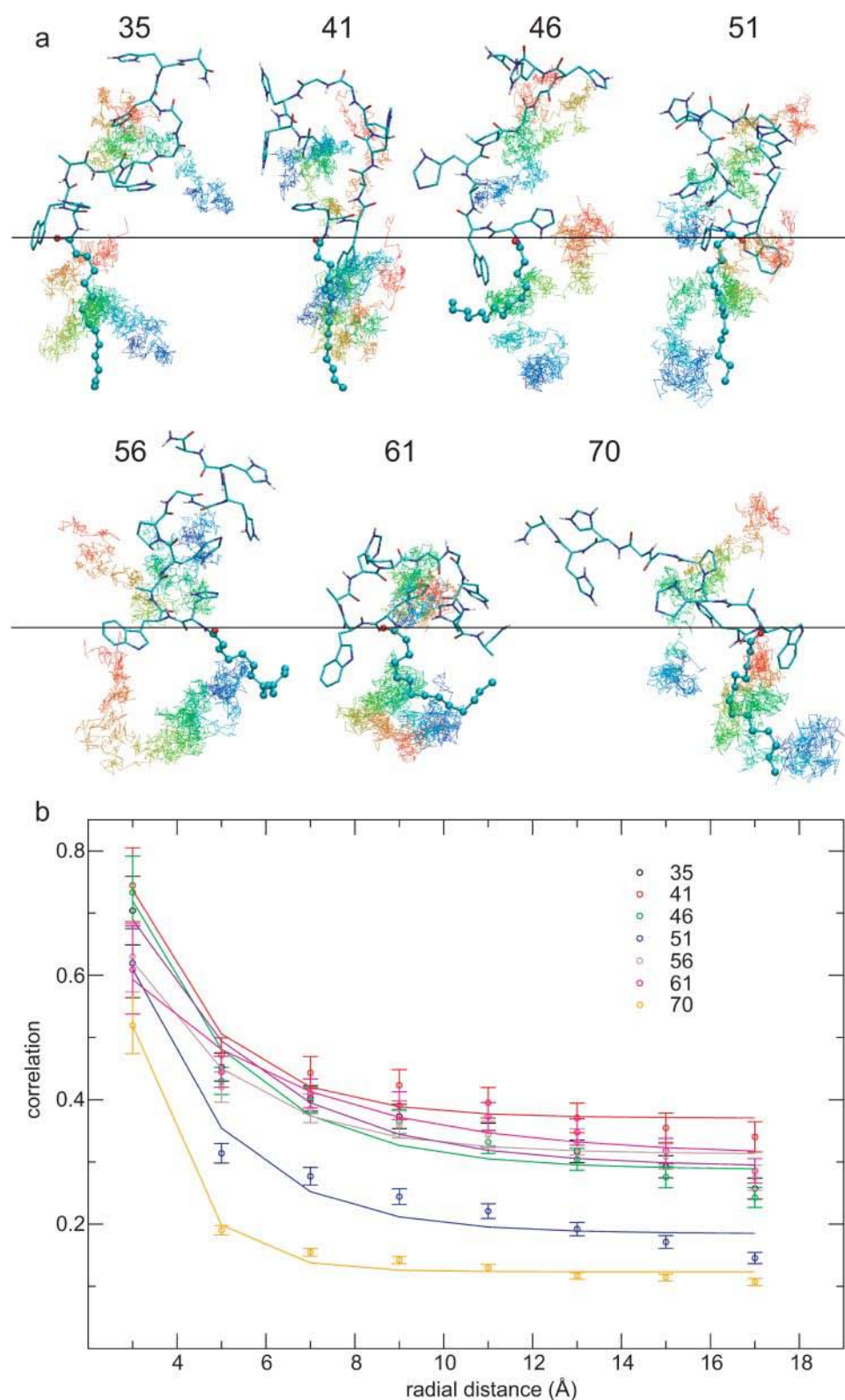
FIGURE 5 Peptide and acyl anchor motions in DPPC$^+$. (*a*) Center-of-mass trajectories of the C$_{14}$-peptide (above *black line*) and the anchor (below *black line*) moieties. The trajectory of each center-of-mass progresses from red to blue with time. Conformations of the C$_{14}$-peptide at the midpoint of the trajectory ($t = 7$ ns, *green-yellow*) appear as reference. The horizontal black lines are guides to the eye indicating approximate location of the lipid membrane. (*b*) Correlation coefficient between the C$_{14}$-peptide and the lipid center-of-mass motion along the membrane normal resolved as a function of radial distance r between the acylated C$_{14}$-peptide and the lipid molecules (see text for more details). The correlation coefficients were calculated from the last 4 ns of the simulations and fitted to a double-exponential function as explained in the text.

$c(r) = \langle \Delta z_P \Delta z_{L(r)} \rangle (\langle \Delta z_P \Delta z_P \rangle \langle \Delta z_{L(r)} \Delta z_{L(r)} \rangle)^{-1/2}$ with $\Delta_i = z_i(t) - z_i(t + \Delta t)$, $i = P$, $L(r)$, and $\Delta t = 10$ ps.

As seen in Fig. 5 *b*, the coupling (correlation) $c(r)$ varies between 0 and 1 for all r, indicating concerted C_{14}-peptide-membrane motions along the bilayer normal. These motions are most concerted nearest the C_{14}-peptide. All correlation functions were fitted to $c(r) = A \exp(-r/r_\alpha) + (1 - A) \exp(-r/r_\beta) + B$. We obtained $r_\alpha = 2.5 \pm 0.7$ Å and $r_\beta = 0.1 \pm 0.3$ Å, which are characteristic length scales of the long-range (mainly electrostatic) interactions and of the short-range (electrostatic + hydrophobic) components of the correlation, respectively. $B = 0.3 \pm 0.1$ should be interpreted as a constant capturing the intrinsic (residual) correlation in the lipid bilayer. Differences observed at the different surface tensions fall within the statistical uncertainties. In the proximity of the C_{14}-peptide, only a few lipid molecules contribute to the calculation of $c(r \rightarrow 0)$ and hence, these values are subject to large uncertainties. However, the fluctuation in $c(r)$ is at $r = 2$ Å relatively small, indicating strong correlation. The correlation between the C_{14}-peptide and membrane dynamics is a direct consequence of the acylation, which strongly integrates the C_{14}-peptide dynamics into the collective motions of the membrane along its normal.

Anisotropy of peptide and anchor motions

To investigate differences in peptide and anchor motion along the membrane normal and membrane plane, respectively, we define average in-plane ($\parallel$) and normal ($\perp$) amplitudes of center-of-mass motions as

$$|A_\parallel| = \left(N_t^{-1} \sum_t^{N_t} [x(t) - \langle x \rangle]^2 + [y(t) - \langle y \rangle]^2 \right)^{1/2} \quad (4)$$

and

$$|A_\perp| = \left(N_t^{-1} \sum_t^{N_t} [z(t) - \langle z \rangle]^2 \right)^{1/2}. \quad (5)$$

The anisotropy $\sigma^A = |A_\parallel| - |A_\perp|$ has its RMS fluctuation $\delta\sigma^A$ defined as

$$\delta\sigma^A = \left(N_t^{-1} \sum_t^{N_t} [\sigma^A(t) - \langle \sigma^A \rangle]^2 \right)^{1/2}. \quad (6)$$

Hence, we obtain simple measures for the extent of the spatial motion of the acylated peptide and its anchor. In Eqs. 4–5, the time averaged center-of-mass projections $\langle x \rangle$, $\langle y \rangle$, and $\langle z \rangle$ are given as $\langle s \rangle = N_t^{-1} \sum_t^{N_t} \sum_i^{N_i} m_i s_i(t) / \sum_i^{N_i} m_i$ with $s = \{x, y, z\}$. $N_t (=8000)$ and N_i is the number of configurations considered and the number of peptide/anchor atoms (of mass m_i), respectively. Similarly, $\sigma^A(t) = [x^2(t) + y^2(t)]^{1/2} - [z^2(t)]^{1/2}$ and $\langle \sigma^A \rangle = N_t^{-1} \sum_t^{N_t} |A_\parallel(t)| - |A_\perp(t)|$ are instantaneous and time-averaged anisotropies in Eq. 6, respectively.

Results obtained at the different surface tensions are summarized in Table 2. Although not optimal, the center-of-mass is a simple collective coordinate when quantifying global motion of the peptide. The data presented do not exhibit any obvious variation of either the motion or the anisotropy with applied surface tension. This indicates that the peptide at all applied tensions is both peripherally and interfacially in contact with the membrane and that an equilibrium between these two contacts modes cannot be reached by the present accessible timescales of MD. For $\gamma = 56$ and 61 dyn/cm, where bilayer lateral areas are reasonable (see Table 1, discussed further below) the peptide and anchor anisotropies are relatively small yet positive implying that the peptide (and its anchor), despite its attachment, is able to move in a direction normal to the membrane plane to a slightly lesser extent than parallel to the membrane plane. However, the observed differences are subject to large statistical uncertainties (see $\delta\sigma^A$, Table 2).

Membrane properties in DPPC$^{\pm}$

In this section we present DPPC$^{\pm}$ results obtained in NP_zAT and $NP_z\gamma T$ ensembles quantifying how the

TABLE 2   Average amplitudes ($A_\parallel$, $A_\perp$), anisotropy (σ^A), and root mean-square fluctuation in σ^A ($\delta\sigma^A$) of the projected center-of-mass movement of the C_{14}-peptide and its acyl anchor from simulations of DPPC$^+$ with applied surface tensions (γ) of 35, 41, 46, 51, 56, 61, and 70 dyn/cm

	Peptide				Anchor			
γ (dyn/cm)	$A_\parallel$ (Å)	$A_\perp$ (Å)	σ^A (Å)	$\delta\sigma^A$ (Å)	$A_\parallel$ (Å)	$A_\perp$ (Å)	σ^A (Å)	$\delta\sigma^A$ (Å)
35	3.59	1.44	2.15	1.57	2.20	2.28	−0.08	2.41
41	2.20	2.28	−0.08	2.41	1.89	2.32	−0.42	2.11
46	3.00	1.41	1.59	1.83	3.69	2.26	1.44	2.82
51	2.59	2.49	0.11	1.84	2.35	2.52	−0.17	1.95
56	2.00	1.49	0.52	1.48	1.94	1.17	0.77	1.18
61	4.42	1.57	2.86	2.85	2.32	2.09	0.23	1.80
70	3.97	4.54	−0.57	1.98	1.98	3.08	−1.10	2.20

We corrected for center-of-mass motion of the total system in the calculations. See text and Eqs. 4–6 for details. The amplitudes might be biased by the fact that the C_{14}-peptide occasionally undergoes structural transitions, which could shift the C_{14}-peptide center-of-mass position. However, since the C_{14}-peptide center-of-mass motion and its anisotropy to some extent correlate with the corresponding quantities of the anchor, which also undergoes structural transitions but with only small changes in center-of-mass position, the results for the C_{14}-peptide predominantly reflect its molecular motion.

membrane-anchored peptide modulates the bilayer lateral compressibility.

Equilibrium area and conjugate surface tension in DPPC⁻

For a small bilayer system, as the present one, constant surface tension simulations constitute a reliable route for determining lateral compressibility moduli (Feller and Pastor, 1999), and hence for studying aspects of the membrane mechanics. We used the NP_zAT ensemble to estimate the surface tension required to reproduce the experimentally determined area per molecule (see Methods). In contrast to the NP_zAT ensemble where density changes are restricted (Zhang et al., 1995), we studied the effect of the peptide on the bilayer lateral compressibility modulus in the $NP_z\gamma T$ ensemble where the system can laterally expand against a constant pressure while allowing for smooth insertion of the peptide into the membrane.

For a fixed area of 62.9 Å² per molecule in the DPPC⁻ simulation, we find (Eq. 1) $\bar{\gamma} = 40.6 \pm 15.8$ dyn/cm, using the last ns of the 2-ns simulation for averaging. This value is close to $\bar{\gamma} = 35 \pm 8$ dyn/cm obtained previously in a relatively short (1-ns) simulation by imposing the same constant area, by using the CHARMM22 parameter set, and by applying a simulation protocol similar to the present one (Feller et al., 1997a). The calculated value of the surface tension, $\bar{\gamma}$ is subject to substantial standard errors, as pointed out elsewhere (Feller et al., 1997a). The large standard errors arise because the pressure tensor components fluctuate substantially. We estimated the standard deviation in the calculated surface tension by using a block-average approach (Flyvbjerg and Petersen, 1989). Here, we calculated average values for $\bar{\gamma}$ within five 200-ps windows and estimated the fluctuation in $\bar{\gamma}$ as fluctuations among these average values. The number (n) of five windows was estimated from a $\sigma^{\bar{\gamma}_n}$ vs. n curve requiring $d\sigma^{\bar{\gamma}_n}/dn = 0$ for proper choice of n.

We note that our computed value of γ fluctuates even more than 8 dyn/cm as estimated earlier (Feller et al., 1997a). This is probably due to the fact that we do not constrain the high frequency bonds to hydrogen atoms and approach longer simulation times. Thus, our (atomic) pressure tensor components (virial) fluctuations exceed 8 dyn/cm, whereas the average value agrees with previous data (Feller et al., 1997a). The value $\gamma = 61$ dyn/cm, which exceeds the upper bound of $\bar{\gamma}$ predicted from the NP_zAT simulation, yields an area per molecule of 62.2 ± 1.5 Å² (Table 1), which, within statistical uncertainties, equals the experimental area per molecule (62.9 Å²).

Membrane elastic properties in DPPC±

We now examine the lateral area and lateral compressibility modulus, K_A, in DPPC±. Whereas the area per DPPC molecule in DPPC⁻ has been determined experimentally to be 62.9 Å²/molecule ($T = 323$ K; Nagle et al., 1996), the experimental value for K_A has not been determined for this type of bilayer; for a recent review of available elastic moduli see Kim and Needham (2002). The area compressibility of DMPC, a lipid molecule whose acyl chains are two carbon atoms shorter than the DPPC molecules of the present study, has been determined to be 140 dyn/cm using pipette aspiration techniques (Evans and Rawicz, 1990; Kim and Needham, 2002). However, the theory used to interpret these experiments seems inadequate, implying that the experimental values reported are probably too low (Henriksen and Ipsen, 2003). Nevertheless, this experimental value for DMPC is presently the most appropriate one to use in the comparison with K_A calculated for DPPC (Feller et al., 1997b; Lindahl and Edholm, 2000). Here we assume that it will only be marginally smaller due to the increased thickness of DPPC relative to DMPC.

We might calculate K_A directly from areas and area fluctuations using Eq. 3. This procedure, however, is for statistical reasons known to yield compressibility moduli that significantly exceed the experimental values (Feller and Pastor, 1999). Furthermore, the value of K_A is also affected by the system size, since long wave-length fluctuations in the bilayer are not captured in the simulations—which leads to an underestimation of the area fluctuations in Eq. 3 (Lindahl and Edholm, 2000; Feller and Pastor, 1999; Marrink and Mark, 2001).

In Figs. 6 and 7 we show the results obtained from our $NP_z\gamma T$ simulations of DPPC±. Fig. 6 displays DPPC+ snapshots obtained with $\gamma = 35, 61$, and 70 dyn/cm taken at $t = 0, 7$, and 14 ns. Fig. 7, a and b, display the DPPC± areas obtained for different surface tensions as a function of time. Fig. 7 c shows the average area (computed within the time interval 10–14 ns) as a function of applied tension. One recognizes from Fig. 6 that an ordered and laterally compact bilayer, very similar to the NPT data in Fig. 2, a–c, results for $\gamma = 35$ dyn/cm after ~7 ns. In contrast, tensions of 61 and 70 dyn/cm produce a fluid, disordered, and laterally expanded bilayer albeit more slowly converging—i.e., lateral expansion still occurs between 7 and 14 ns, with DPPC+ at $\gamma = 70$ dyn/cm ending up being overstretched at $t = 14$ ns.

Fig. 7, a and b, illustrates that area equilibrium areas are difficult to extract even in DPPC⁻. At lower tensions ($\gamma \leq 51$ dyn/cm), the convergence onset in DPPC+ resembles that in DPPC⁻. In contrast, for DPPC+ convergence is slower at larger tensions (56, 61, and 70 dyn/cm) than for DPPC⁻. Toward the end of these three simulations, C_{14}-peptide-bilayer electrostatic interactions in DPPC+ become very stable (data not shown), which modulates the lateral response (stretch) of the bilayer to the applied tension. Given that the correct area per molecule in DPPC⁻ is obtained for 61 dyn/cm (Table 1), we choose for consistency reasons DPPC+ with 61 dyn/cm when quantifying, relative to DPPC⁻,
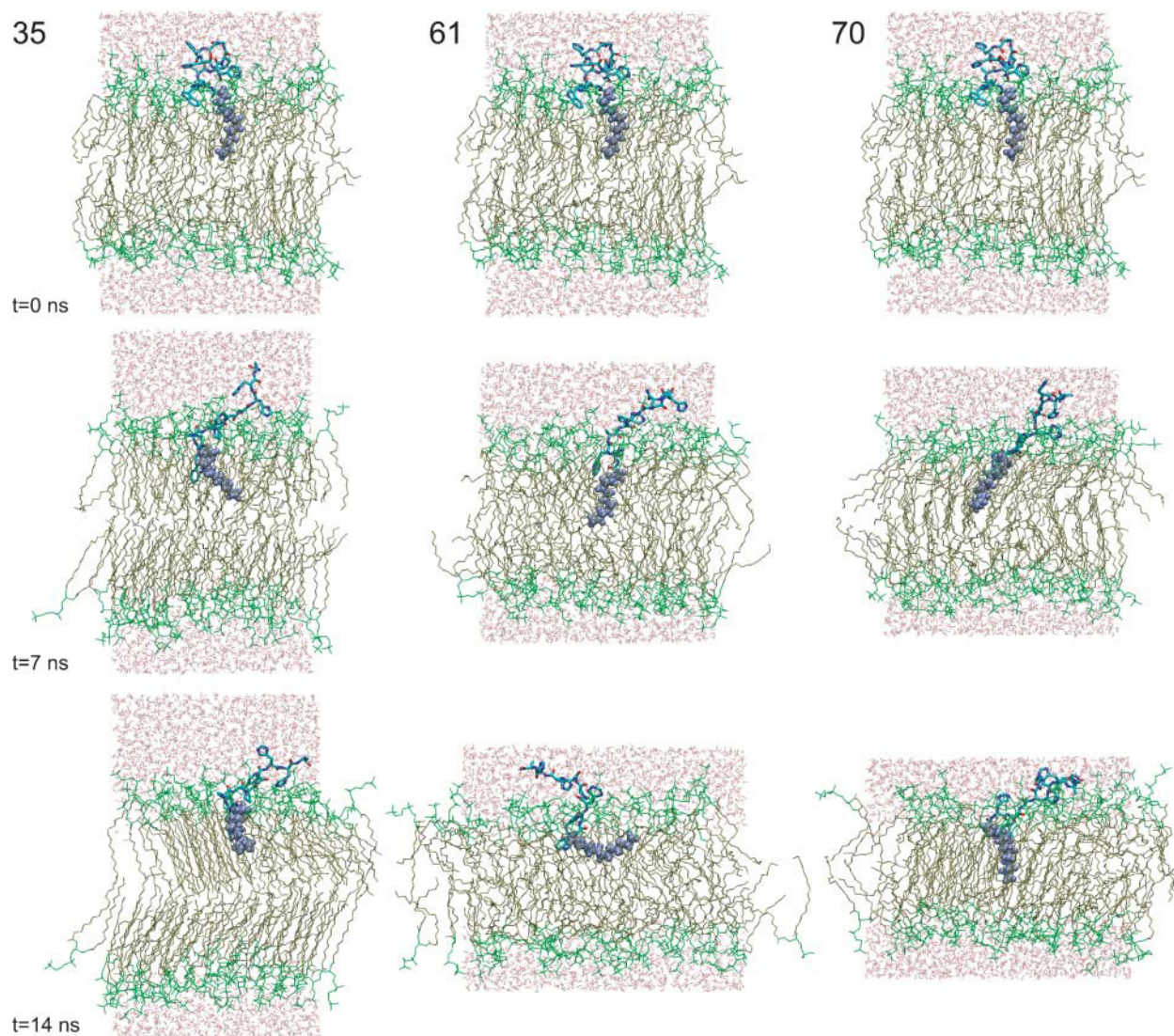
FIGURE 6 Snapshots taken at $t = 0$ ns, 7 ns, and 14 ns of DPPC$^+$ simulated in the $NP_z\gamma T$ ensemble with $\gamma = 35$, 61, and 70 dyn/cm. Water molecules are shown in red (O) and white (H), and the C$_{14}$-peptide and its anchor is displayed in licorice and as gray van der Waals spheres, respectively. The lipid headgroup and the aliphatic part of the membrane are represented in green and brown, respectively. In contrast to the NPT simulations (compare to Fig. 2), ordering and tilt of the lipid acyl chains are preserved with simulation time for $\gamma = 61$ and 70 dyn/cm, whereas application of a surface tension of 35 dyn/cm is insufficient to prevent the membrane from becoming crystalline as in the NPT simulations (see Fig. 2). The overall bilayer thickness decreases with time when the two larger surface tensions are applied.

changes in bilayer structure due to the presence of the C$_{14}$-peptide.

A lateral compressibility modulus in agreement with experiment is obtained from Fig. 7 c using the slope ($= A_0/K_A$) provided by linear regression of the plot of $\bar{A}$ vs. γ (see Fig. 7 c and Eq. 2; see also Feller and Pastor, 1999). We obtain as mean $K_A = 134$ dyn/cm with lower and upper bounds of 103 dyn/cm and 191 dyn/cm, respectively, using the experimentally determined area per molecule; $A_0 = 62.9$ Å^2/molecule. Our K_A compares well with the experimental (DMPC) modulus of 140 dyn/cm (Evans and Rawicz, 1990; Kim and Needham, 2002) and due to the longer timescale

deployed here, is more reliable than the $K_A = 360$ dyn/cm previously reported (Feller and Pastor, 1999), given the long relaxation time needed for the bilayer to respond to the applied tension.

Increasing the surface tension implies that the membrane is laterally expanded (see Figs. 6 and 7). As expected, this is borne out in our DPPC$^-$ results where the area increases with increasing surface tension. For DPPC$^+$ the area change occurring with largest γ (70 dyn/cm) implies that the membrane is overstretched, recalling here that $\gamma = 61$ dyn/cm reproduces the experimental area per molecule in DPPC$^-$ and we therefore assume this to be the appropriate tension for
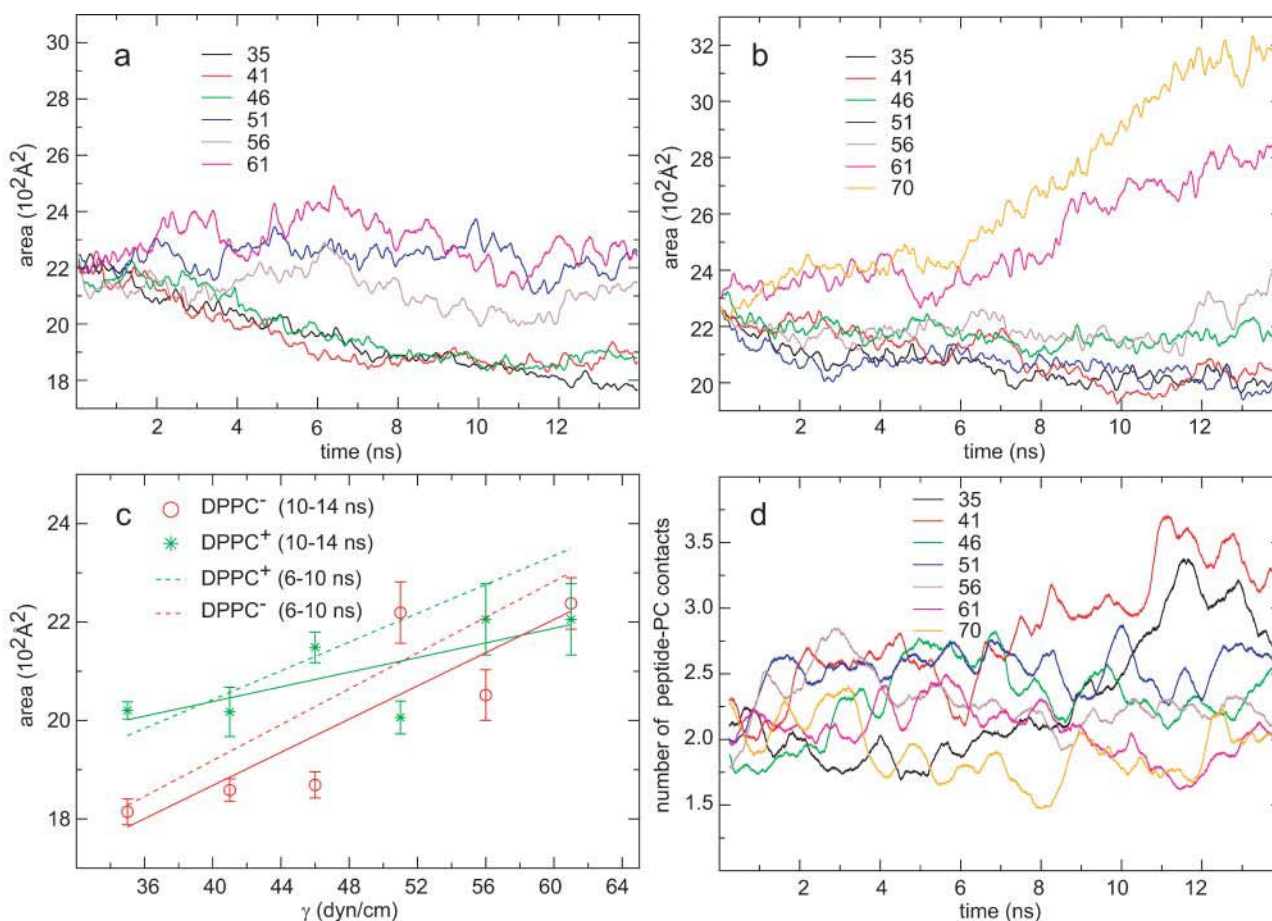
FIGURE 7 (a) Total areas for the DPPC$^-$ obtained with $\gamma = 35, 41, 46, 51, 56$, and 61 dyn/cm (given in the *inset*) as a function of simulation time. (b) Same for DPPC$^+$ with $\gamma = 70$ dyn/cm in addition. (c) Projected total area as a function of applied surface tension for DPPC$^+$ and DPPC$^-$ along with a linear regression of the computed average areas. Average areas and average area fluctuations were calculated in the interval 10–14 ns (see *a* and *b*) using block averaging as described in the text. For DPPC$^-$ linear regression was performed in the full range of applied tension. For DPPC$^+$, linear regression includes data up to $\gamma = 61$ dyn/cm only since the membrane becomes overstretched for $\gamma = 70$ dyn/cm (average area not shown; see text, Table 1, and Fig. 6 for further details). Linear regression of average areas calculated using the block average procedure over the time intervals 6–10 ns is included for DPPC$^\pm$ to illustrate how calculated compressibilities depend on simulation time (see Eqs. 2 and 3 and text for discussion). Panel *d* displays the number of C$_{14}$-peptide-lipid headgroup (*PC*) contacts as a function of simulation time in DPPC$^+$.

DPPC$^+$ as well. Considering the areas of DPPC$^+$ obtained for $\gamma = 35$–61 dyn/cm, these increase reasonably linearly with γ in this interval, with an exception being $\gamma = 51$ dyn/cm—suggesting that constant surface tension simulations might eventually lead to kinetically trapped nonglobal area minima.

The resulting slope of the linear regression of the $\bar{A}$ vs. γ plot of DPPC$^+$ differs from that of DPPC$^-$ (Fig. 7 *c*). The resulting compressibility for DPPC$^+$ is 444 dyn/cm with upper and lower bounds of 809 and 306 dyn/cm, respectively. In determining K_A for DPPC$^+$ we utilized the ratio between the extrapolated areas $[A'_0(\text{DPPC}^+)/A'_0(\text{DPPC}^-)]_{\gamma \to 0} = 1.5$ and employed the experimental area for DPPC$^-$. Despite use of this estimate, these findings imply that DPPC$^+$ becomes moderately stiffer (K_A increases).

C_{14}-peptide-membrane contacts and lateral area expansions

The increase in K_A in DPPC$^+$ relative to DPPC$^-$ is dictated by the large change in equilibrium area although the exact magnitude of this change is poorly determined in our simulations despite the relatively long timescales even for current standards. To gauge the relaxation times needed to arrive at final estimates for changes in K_A, we also computed the compressibilities from average areas extracted over the time interval 6–10 ns. As seen from Fig. 7, *a*–*c*, the calculated K_A for DPPC$^-$ is relatively unchanged with mean, lower, and upper bounds of 124 dyn/cm, 112 dyn/cm, and 170 dyn/cm, respectively, noting that the slope in Fig. 7 *c* remains constant in these two time intervals whereas the equilibrium area decreases. In contrast, the compressibilities for DPPC$^+$ changes significantly from the first to the second

time interval; 190, 142, and 287 dyn/cm are mean, lower and upper bounds, respectively, for K_A, which is significantly lower than the K_A-values derived above over the time interval 10–14 ns (compare to Fig. 7 c). This difference originates in a slow response of the membrane to the presence of a C_{14}-peptide at its interface where concurrent lateral area expansions ultimately change the slope in the $\bar{A}$ vs. γ-graph (Fig. 7 c).

The origin of this change is further analyzed in Fig. 7 d by displaying the number of atom-atom contacts (within a threshold of 3 Å) between the C_{14}-peptide and the lipid headgroup as a function of time. The data are normalized by the number of PC headgroup atoms (34 per headgroup). The contacts number is between 1.5 and 3 and it varies strongly with time indicating that the C_{14}-peptide is mobile at the surface. It increases with time for $\gamma \lesssim 51$ dyn/cm whereas for $\gamma \gtrsim 56$ dyn/cm the contact number is essentially the same at $t = 0$ and $t = 14$ ns, i.e., at lower surface tensions C_{14}-peptide insertion seems severely hindered by a too compact bilayer. The insertion of the C_{14}-peptide into the lipid interface is in part also hampered by displacement of water at the lipid-water interface. This is indicated by the complementary finding that the number of lipid water hydrogen bonds continuously decreases over the first 10 ns in all systems whereas the number of lipid–C_{14}-peptide hydrogen bonds correspondingly increases (data not shown).

C_{14}-peptide-lipid interactions in DPPC$^+$

In this section we describe the interactions between the C_{14}-peptide and the lipid bilayer and quantify changes in bilayer structural ordering occurring upon peptide anchoring.

The C_{14}-peptide-lipid interface

Our peptide has a Trp residue (Trp^2). Trp has been suggested to have preference for the lipid headgroup region with a tendency to locate toward the hydrophobic part of the membrane (Tieleman and Berendsen, 1998; Aliste et al., 2003). Trp has been attributed various functions in membrane proteins including, e.g., a role as a determinant in protein translocation along membranes (Schiffer et al., 1992). However, detailed examination of average Trp orientations and distributions obtained from MD simulations of several transmembrane proteins and peptides produced little convincing evidence for that particular function (Tieleman and Berendsen, 1998). Trp^2 in our C_{14}-peptide is positioned close to the acyl anchor. To examine the interfacial location of the C_{14}-peptide, we calculated the average distribution of its center-of-mass and atomic distributions of the complete C_{14}-peptide, of Trp^2, and of the PC headgroup for DPPC$^+$ with $\gamma = 61$ dyn/cm (Fig. 8 a).

The C_{14}-peptide distribution reveals that the C_{14}-peptide is located at the interfacial region (penetration depth varies noncharacteristically with surface tension; data not shown).

The Trp^2 distribution is broad and the side chain is consistently located within the region spanned by lipid headgroup and the hydrophobic core of the membrane indicating that Trp^2 is flexible but at the same time its position relative to the lipid bilayer is well defined. Trp^2 together with the acyl anchor contribute to anchoring of the C_{14}-peptide, which is consistent with fluorescence experiments (Pedersen et al., 2001a,b). We cannot distinguish between the individual contributions of Trp^2 and the acyl anchor to the overall anchoring strength, since the Trp^2 position overlaps with that of the acyl chain and is predetermined by the hydrophobic anchor. However, the fluorescence experiments indicated that Trp^2 alone cannot anchor the peptide (Pedersen et al., 2001a,b).

Orientation of tryptophan and histidine residues

As suggested by Tieleman and co-workers the Trp orientation can be characterized by two order parameters, $S_n = 1/2(3\cos^2(\alpha)-1)$ and $S_l = 1/2(3\cos^2(\beta)-1)$, describing orientation of the ring-normal and of the ring long-axis, respectively (Tieleman and Berendsen, 1998; Aliste et al., 2003). Similarly, we have applied S_n and S_l to characterize the orientation of His side chains. Fig. 8 b displays a simulation snapshot with a typical Trp orientation and the two vectors used in defining S_n and S_l (see also Figs. 4 c, 5 a, and 6). In S_n, $\cos(\alpha)$ is the projection of the ring normal onto the outgoing bilayer normal (**n**). $S_n = -0.5$ indicates an orientation of the ring perpendicular to the membrane plane. $S_n = 1$ implies that the ring aligns along the membrane plane. Correspondingly, $\cos(\beta)$ is the projection of the C_γ–C_β bond vector onto **n**. $S_l = -0.5$ implies that the long axis of the ring aligns along the membrane plane. For $S_l = 1$ the long axis aligns along **n** and consequently $S_n = -0.5$.

In Fig. 8 c, S_n and S_l for Trp^2 appear as a function of time for DPPC$^+$ ($\gamma = 61$ dyn/cm). Fluctuations in S_n and S_l illustrate that only small orientational transitions of Trp are possible since the confinement of the Trp ring is strong. As seen from Fig. 8 c, upper panel, S_n for Trp^2 fluctuates ~ -0.5, implying that the ring normal most frequently aligns along the membrane plane and never parallel to it ($f(S_n) \neq 1$), whereas S_l (Fig. 8 c, lower panel) approaches 1, indicating that the long axis most frequently aligns parallel with **n**. Corresponding frequency functions of S_n and S_l ($f(S_i)$, $i = n$, l) for Trp^2 and for His^1, ^{4}, ^{8}, and ^{9} appear in Fig. 8 d. For Trp^2, $f(S_n)$ is clearly skewed toward -0.5 whereas $f(S_l)$ is skewed toward 1, confirming our deduced orientation. We also inspected His orientations (Fig. 8 d). All His residues exhibit preferential orientations but different from that of Trp^2, since His residues mutually interact, i.e., stack and/or participate in intrapeptide hydrogen bonding. For His^1, located between the acyl anchor and Trp^2, $f(S_n)$ is skewed toward 1, whereas $f(S_l)$ is skewed toward -0.5 implying that the imidazole ring and its long axis both lie parallel to the membrane plane. For His^4 $f(S_n)$ is symmetric, i.e., rotations
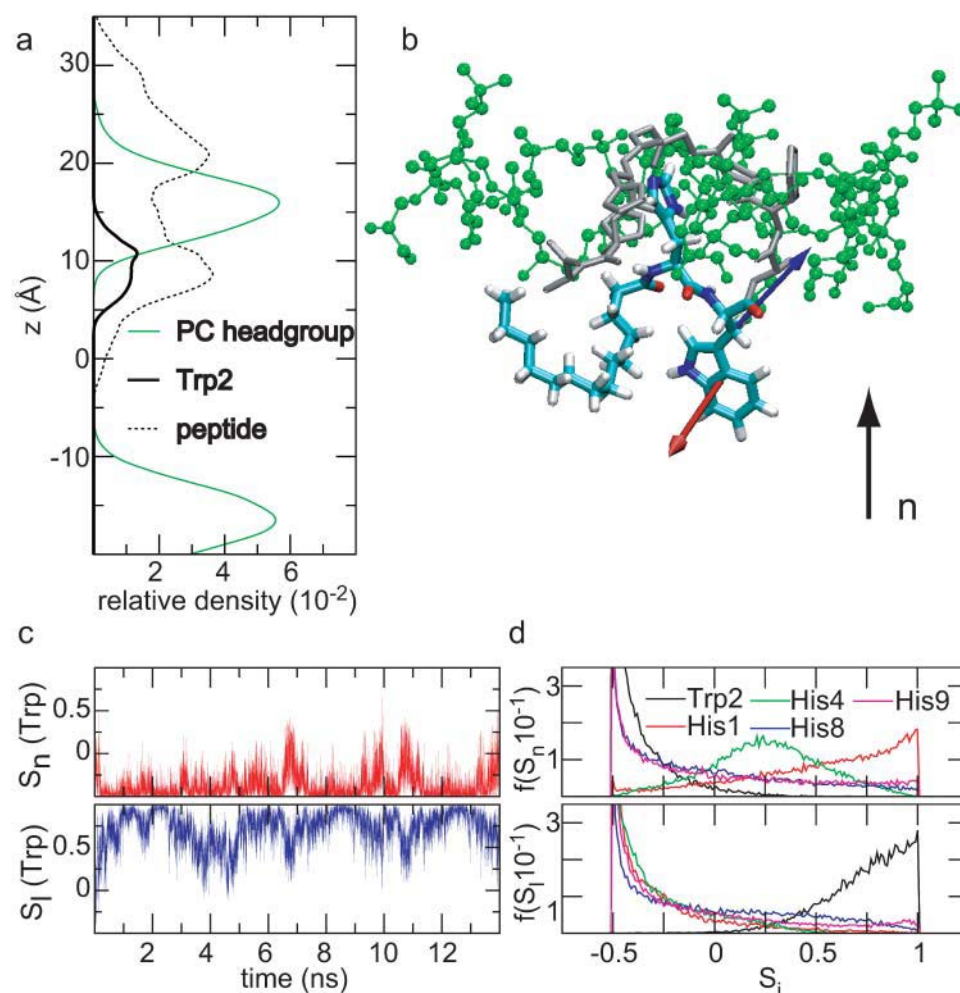
FIGURE 8 (a) Relative distributions of the Trp residue (Trp[2]), the choline lipid headgroup (PC), and of the C_{14}-peptide calculated from the last 4 ns of the simulation of DPPC$^+$ with $\gamma = 61$ dyn/cm. Due to the presence of the C_{14}-peptide in the upper monolayer, the densities are not symmetric around the center-of-mass at $z = 0$ (see also Fig. 6). (b) Snapshot of the C_{14}-peptide located in the lipid-water interface. His[1], Trp[2], and the acyl anchor are highlighted in licorice whereas the remainder of the peptide and the PC headgroups at closest proximity to the C_{14}-peptide are shown in gray and green colors, respectively, while omitting hydrogen atoms. The two vectors defining order parameters S_n and S_1 used to quantify the orientation of Trp[2] upon their projection onto the interfacial normal (**n**) are displayed in red (S_n) and blue (S_1) (see text for definitions of S_n and S_1). (c) Order parameters S_n and S_1 with color-coding matching the vectors in b characterizing the orientation of Trp[2] at the lipid-water interface in DPPC$^+$ with $\gamma = 61$ dyn/cm as a function of time. (d) Frequency functions $f(S_i, i = n, l)$ of S_n and S_1 of Trp[2] in c and of His[1, 4, 8], and [9].

of the ring along the C_γ–C_β bond vector occur whereas the long axis aligns parallel to the membrane plane, i.e., $f(S_1)$ is skewed toward −0.5. Finally, the protonated His[8] and His[9] prefer identical orientations. The values $f(S_n)$ and $f(S_1)$ are skewed toward −0.5 indicating, respectively, that the imidazole ring aligns perpendicular to the membrane plane with the long axis directed along the membrane plane. Correlation functions computed for the angular motion of the Trp ring normal and for the $C\gamma \rightarrow C_\beta$ bond vector suggest that the correlation is highly anisotropic with timescales exceeding several nanoseconds. Given the long timescale no exact value for the angular correlation time can be provided by the simulations (data not shown). Nevertheless these results suggest that anisotropies should be observed in fluorescence experiments, which remains to be addressed.

Lipid ordering—the acyl chains

Radial deformations of the bilayer thickness occurring due to the presence of peripheral or integral membrane proteins as well as peptides and concurrent changes in membrane structure, e.g., in lipid ordering, are commonly associated with the hydrophobic matching postulate (Mouritsen and Bloom, 1984, 1993; Mouritsen and Sperotto, 1993; Mouritsen et al., 1995; Dumas et al., 1999). Perturbation of the lipid membrane due to the C_{14}-peptide also occurs in DPPC$^+$ (Fig. 6). However, due to statistical uncertainties and the dynamic C_{14}-peptide behavior, no accurate measure of bilayer deformation can be extracted. The most significant changes are observed with respect to lipid ordering. Order parameter profiles for the acyl carbon atoms and for the acyl anchor in DPPC$^\pm$ ($\gamma = 61$ dyn/cm) are shown in Fig. 9 a. The DPPC$^-$ results resemble previously reported lipid order parameters for related constant area simulations of DPPC$^-$ (Feller and MacKerell, 2000) and experimental data. Typical features are: 1), a maximum of 0.22 at $\sim C_5 - C_6$; 2), increased disorder toward the bilayer center; and 3), an order parameter plateau around carbons 5–8. These characteristics persist at different applied surface tensions and we find increased disorder with increasing surface tension (see data in Supplementary Material).
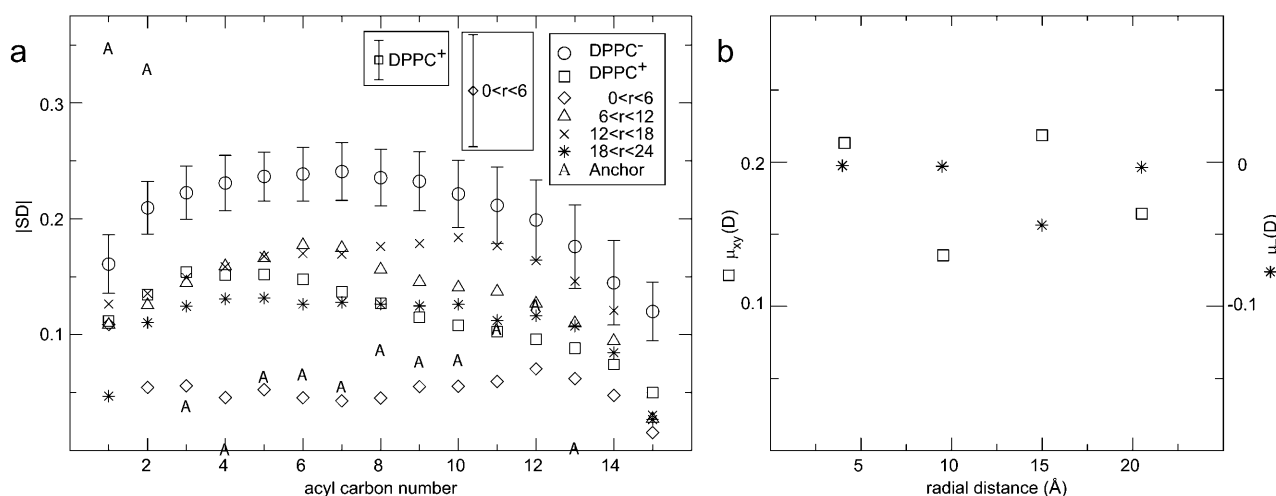
FIGURE 9 (a) Lipid deuterium order parameter profiles ($|SD|$) for DPPC$^+$ with $\gamma = 61$ dyn/cm resolved with radial distance to the C$_{14}$-peptide in 6 Å intervals (see *inset, upper right*, for legend; *left* and *mid insets* are standard deviations). Order parameter profiles in the monolayer in DPPC$^+$ devoid of C$_{14}$-peptide (denoted DPPC$^+$ in the *inset, upper right*) and corresponding order parameter profiles for DPPC$^-$ (with $\gamma = 61$ dyn/cm) are included for comparison. Order parameter profile for the C$_{14}$-acyl anchor (13 acyl carbon atoms) in DPPC$^+$ is included for completeness. (b) In plane (xy) and out of plane (z) average polarization in the PC headgroup region in DPPC$^+$ with $\gamma = 61$ dyn/cm displayed by means of the average P–N dipole components $\boldsymbol{\mu}_{xy} = [\mu_x{}^2 + \mu_y{}^2]^{1/2}$ and μ_z of the PC headgroup, resolved with increasing radial distance to the C$_{14}$-peptide in 6 Å intervals.

For DPPC$^+$ we resolved the order parameter profiles with radial distance to the C$_{14}$-peptide with annuli increasing in intervals of 6 Å (Fig. 9 a). Relative to DPPC$^-$ we find increased disorder, most pronounced in proximity of the C$_{14}$-peptide ($r < 6$ Å) where disorder is maximal at C$_2$–C$_8$. This is induced by the anchor dynamics as well as the curling up of the acyl anchor. Hence, both static and dynamic order of the nearby lipid molecules are affected. For $r > 6$ Å the ordering approaches the DPPC$^-$ reference values at C$_1$ whereas tail disorder persists regardless of r. Even the monolayer devoid of C$_{14}$-peptide (denoted *DPPC$^+$* in Fig. 9 a) exhibits increased disorder relative to DPPC$^-$. However, this difference is not featured at $\gamma = 56$ dyn/cm while our findings above persist at this tension (see data in Supplementary Material), which, as previously discussed, could serve as reference tension for DPPC$^+$ as well. The anchor (represented by poor statistics) exhibits a structureless order parameter profile with no characteristic variation along the acyl chain (regardless of γ; see also data in Supplementary Material) reflecting both strong static and dynamic disorder of the anchor.

Lipid ordering—the lipid headgroup

Since one expects strong electrostatic interactions between the C$_{14}$-peptide and the lipid headgroup to dominate the C$_{14}$-peptide-lipid interactions in the headgroup region, it is of interest to quantify whether the polarization in the lipid headgroup region also varies in a characteristic manner with radial distance from the C$_{14}$-peptide. For DPPC$^+$ with $\gamma = 61$ dyn/cm we computed the average in-plane component of the P–N dipole of the PC headgroups ($\boldsymbol{\mu}_\parallel = \boldsymbol{\mu}_{xy} = [\mu_x{}^2 +$

$\mu_y{}^2]^{1/2}$) as well as the normal component ($\mu_\perp = \mu_z$), Fig. 9 b, with same resolution as applied in the calculation of the lipid acyl order parameters profiles above. Changes in $\boldsymbol{\mu}_\parallel$ and $\mu_\perp$ with r are small. Near the C$_{14}$-peptide ($r < 6$ Å) an increase in $\boldsymbol{\mu}_\parallel$ relative to distant from the C$_{14}$-peptide ($r \gg 6$ Å) is found (persists at all surface tensions, data not shown), which probably is due to rather local interactions between the PC headgroup and the interfacially located His[1] and in part His[4] and Trp[2]. The tendency to localize the C$_{14}$-peptide toward the water region keeps the changes in the P–N polarization modest. Overall, P–N polarization changes due to the C$_{14}$-peptide are much smaller than the corresponding changes in the hydrophobic region. Perhaps this is surprising since one expects electrostatic interactions to be a major determinant for the peptide-lipid interactions in systems such as the present one (Aliste et al., 2003) but we find that, mainly, the acyl anchor affects structural order in the membrane (Fig. 9 a).

CONCLUSION

A C$_{14}$-peptide conformation was obtained from MD simulations. Anchored to a DPPC membrane, the C$_{14}$-peptide exhibits conformational fluctuations that are more pronounced than in aqueous solution and samples relatively large regions of the membrane plane on a 14-ns timescale. The C$_{14}$-peptide remained stable in the simulations in aqueous solution but at the lipid interface it may, on a 14-ns timescale, undergo reversible conformational transitions. Strong coupling between the C$_{14}$-peptide and the membrane dynamics was observed and the C$_{14}$-peptide behaves via its anchor as an integral part of the membrane.

The conformational freedom exhibited by the C_{14}-peptide despite its anchor might be relevant for studies of receptor-peptide interactions. Besides prolonging receptor-peptide interactions, acylation is found not to abolish peptide conformational flexibility and it only moderately affects the bilayer elastic properties. Our results show that the lateral compressibility modulus increases due to the presence of the C_{14}-peptide. The average Trp location in our simulations suggests that the C_{14}-peptide associates to the interface in accordance with observed fluorescence energy transfer between Trp and a fluorescence probe located in the hydrophobic core of the membrane manifesting the anchoring role of Trp (Pedersen et al., 2001a,b).

Finally, our *NPT* results on pure lipid bilayers, which to the best of our knowledge are the only multiple nanosecond, *NPT* simulations of DPPC bilayers with the CHARMM27 parameter set reported, advocate against use of the CHARMM27 parameter set in lipid bilayer simulations with constant ambient pressure, since it results in bilayers that are too compact. Before being used with constant pressure the CHARMM27 parameter set therefore needs adjustment despite recent improvements quantified in terms of order parameters and *trans/gauche* transitions (Feller and MacKerell, 2000). For future improvement and performance evaluation of the parameter set, the *NPT* ensemble must be adopted in addition to the NP_zAT ensemble since *NPT* ensembles are preferred over the NP_zAT ensemble in lipid-protein simulations, where equilibrium densities are unknown (Zhang et al., 1995). We previously conducted *NPT* and NP_zAT simulations of long (C_{36}) alkane molecules, and found excellent agreement with x-ray data; electron density profiles and areas per molecule were reproduced in both ensembles (Jensen et al., 2003, 2004), manifesting that the CHARMM27 parameter set under ambient pressure conditions performs inadequately in the headgroup region rather than in the alkane chain region.

SUPPLEMENTARY MATERIAL

An online supplement to this article can be found by visiting BJ Online at http://www.biophysj.org.

REFERENCES

Alexov, E. G., and M. Gunner. 1997. Incorporating protein conformational flexibility into the calculation of pH-dependent protein properties. *Biophys. J.* 72:2075–2093.

Aliste, M. P., J. L. MacCallum, and D. P. Tieleman. 2003. Molecular dynamics simulations of pentapeptides at interfaces: salt bridge and cation-π interactions. *Biochemistry*. 42:8976–8987.

Allen, M. P., and D. J. Tildesley. 1988. Computer Simulation of Liquids. Clarendon, Oxford, UK.

Åman, K., E. Lindahl, O. Edholm, P. Håkansson, and P.-O. Westlund. 2003. Structure and dynamics of interfacial water in an L_α phase lipid bilayer from molecular dynamics simulations. *Biophys. J.* 84:102–115.

Antosiewicz, J., J. McCammon, and M. Gilson. 1994. The determinants of pK_as in proteins. *J. Mol. Biol.* 238:415–436.

Bashford, D., and M. Karplus. 1990. PK_as of ionizable groups in proteins: atomic detail from a continuum electrostatic model. *Biochemistry*. 29:10219–10255.

Berendsen, H., R. van der Spoel, and D. van Drunen. 1995. GROMACS: a message-passing parallel molecular dynamics implementation. *Comp. Phys. Comm.* 91:43–56.

Berendsen, H. J. C., J. R. Grigera, and T. P. Straatsma. 1987. The missing term in effective pair potentials. *J. Phys. Chem.* 91:6269–6271.

Berger, O., E. Edholm, and F. Jähnig. 1997. Molecular dynamics simulations of a fluid bilayer of dipalmitoylphosphatidylcholine at full hydration, constant pressure and constant temperature. *Biophys. J.* 72:2002.

Beroza, P., and D. Case. 1996. Including side chain flexibility in continuum electrostatic calculations of protein titration. *J. Phys. Chem.* 100:20156–20163.

Darden, T., D. York, and L. Pedersen. 1993. Particle Mesh Ewald: an N log(N) method for Ewald sums in large systems. *J. Chem. Phys.* 98:10089–10092.

Davis, M., J. Madura, B. Luty, and J. McCammon. 1991. Electrostatic and diffusion of molecules in solution: simulations with the University of Houston Brownian Dynamics Program. *Comp. Phys. Comm.* 62:187–197.

Davis, M., and J. McCammon. 1991. Dielectric boundary smoothing in finite difference solutions of the Poisson equation: an approach to improve accuracy and convergence. *J. Comp. Chem.* 7:909–912.

Dell'Aqua, M. L., M. C. Faux, J. Thorburn, A. Thorburn, and J. D. Scott. 1998. Membrane-targeting sequences on AKAP79 bind phosphatidylinositol-4,5-bisphosphate. *EMBO J.* 17:2246–2260.

Dell'Aqua, M. L., and J. D. Scott. 1997. Protein kinase A anchoring. *J. Biol. Chem.* 272:12881–12884.

Dumas, F., M. C. Lebrun, and J.-F. Tocanne. 1999. Is the protein/lipid hydrophobic matching principle relevant to membrane organization and functions? *FEBS Lett.* 458:271–277.

Essmann, U., L. Perera, M. L. Berkowitch, T. Darden, L. Hsing, and L. G. Pedersen. 1995. A smooth particle mesh Ewald method. *J. Chem. Phys.* 103:8577–8593.

Evans, E., and W. Rawicz. 1990. Entropy driven tension and bending elasticity in condensed-fluid membranes. *Phys. Rev. Lett.* 64:2094–2097.

Faux, M., and J. Scott. 1996. More on target with protein phosphorylation: conferring specificity by location. *TIBS*. 21:312–315.

Feller, S. E., and A. MacKerell. 2000. An improved empirical potential energy function for molecular simulations of phospholipids. *J. Phys. Chem. B*. 104:7510–7515.

Feller, S. E., and R. W. Pastor. 1999. Constant surface tension simulations of lipid bilayers: the sensitivity of surface areas and compressibilities. *J. Chem. Phys.* 111:1281–1287.

Feller, S. E., R. M. Venable, and R. W. Pastor. 1997a. Computer simulation of a DPPC phospholipid bilayer: structural changes as a function of molecular surface area. *Langmuir*. 13:6555–6561.

Feller, S. E., D. Yin, R. W. Pastor, and A. D. MacKerell, Jr. 1997b. Molecular dynamics simulation of unsaturated lipids at low hydration: parameterization and comparison with diffraction studies. *Biophys. J.* 73:2269–2279.

Feller, S. E., Y. H. Zhang, R. W. Pastor, and B. R. Brooks. 1995. Constant pressure molecular dynamics simulation—the Langevin piston method. *J. Chem. Phys.* 103:4613–4621.

Flyvbjerg, H., and H. G. Petersen. 1989. Error estimates on averages of correlated data. *J. Chem. Phys.* 91:461–466.

Gesell, J., M. Zasloff, and S. J. Opella. 1997. Two-dimensional ^{1}H NMR experiments show that the 23-residue magainin antibiotic peptide is an α-helix in dodecylphosphocholine micelles, sodium dodecylsulfate micelles, and trifluoroethanol/water solution. *J. Biomol. NMR.* 2:127–135.

Gilson, M. 1993. Multiple-site titration and molecular modeling: two rapid methods for computing energies and forces for ionizable groups in proteins. *Proteins Struct. Funct. Gen.* 15:266–282.

Gorfe, A., P. Ferrara, A. Caflish, D. Marti, H. Bosshard, and I. Jelesarov. 2002. Calculation of protein ionization equilibria with conformational sampling: pK_a of a model leucine zipper, gcn4 and barnase. *Proteins.* 46:41–60.

Henriksen, J. R., and J. H. Ipsen. 2003. Measurement of membrane elasticity by micropipette aspiration. *Eur. Biophys. J.* In press.

Hess, B., H. Bekker, H. J. C. Berendsen, and J. G. E. M. Fraaije. 1997. LINCS: a linear constraint solver for molecular simulations. *J. Comp. Chem.* 1463–1472.

Humphrey, W., A. Dalke, and K. Schulten. 1996. VMD—visual molecular dynamics. *J. Mol. Graph.* 14:33–38.

Jensen, T. R., M. Ø. Jensen, N. Reitzel, K. Balashev, G. H. Peters, K. Kjaer, and T. Bjørnholm. 2003. Water in contact with extended hydrophobic surfaces: direct evidence of weak dewetting. *Phys. Rev. Lett.* 90:0861011–08601014.

Jensen, M. Ø., O. G. Mouritsen, and G. H. Peters. 2004. The hydrophobic effect: molecular dynamics simulations of water confined between extended hydrophobic and hydrophilic surfaces. *J. Chem. Phys.* 120:9729–9744.

Jorgensen, W. L., J. Chandrasekhar, J. D. Medura, R. W. Impey, and M. L. Klein. 1983. Comparison of simple potential models for simulating liquid water. *J. Chem. Phys.* 79:926–935.

Kabsch, W., and C. Sander. 1983. Direction of protein secondary structure: pattern recognition of hydrogen bonded and geometrical features. *Biopolymers.* 22:2577–2637.

Kalé, L., R. Skeel, M. Bhandarkar, R. Brunner, A. Gursoy, N. Krawetz, J. Phillips, A. Shinozaki, K. Varadarajan, and K. Schulten. 1999. NAMD2: greater scalability for parallel molecular dynamics. *J. Comp. Phys.* 151:283–312.

Kim, D., and D. Needham. 2002. Lipid bilayers and monolayers: characterization using micropipette manipulation techniques. *In* Encyclopedia of Surface and Colloid Science. A. Hubbard, editor. Marcel Dekker, New York. 3057–308.

Kurtzhals, P., S. Havelund, I. Jonassen, B. Kiehr, U. Ribel, and J. Markussen. 1996. Albumin binding and time action of acylated insulins in various species. *J. Pharma. Sci.* 85:304–308.

La Rocca, P., P. C. Biggin, D. P. Tieleman, and M. S. P. Sansom. 1999. Simulation studies of the interaction of antimicrobial peptides and lipid bilayers. *Biochim. Biophys. Acta.* 1462:185–200.

Lemmich, J., K. Mortensen, J. H. Ipsen, T. Hønger, R. Bauer, and O. G. Mouritsen. 1996. Small angle neutron scattering from multilamellar lipid bilayers: theory, model, and experiment. *Phys. Rev. E.* 53:5169–5180.

Lindahl, E., and O. Edholm. 2000. Mesoscopic undulations and thickness fluctuations in lipid bilayers from molecular dynamics simulations. *Biophys. J.* 79:426–433.

Lindahl, E., B. Hess, and D. van der Spoel. 2001. GROMACS 3.0: a package for molecular simulation and trajectory analysis. *J. Mol. Model.* 7:306–317.

MacKerell, Jr., A. D., D. Bashford, M. Bellott, R. Dunbrack, Jr., J. Evanseck, M. Field, S. Fischer, J. Gao, H. Guo, S. Ha, D. Joseph-McCarthy, L. Kuchnir, K. Kuczera, F. Lau, C. Mattos, S. Michnick, T. Ngo, D. Nguyen, B. Prodhom, W. Reiher III, B. Roux, M. Schlenkrich, J. Smith, R. Stote, J. Straub, M. Watanabe, J. Wiorkiewicz-Kuczera, D. Yin, and M. Karplus. 1998. All-atom empirical potential for molecular modeling and dynamics studies of proteins. *J. Phys. Chem. B.* 102:3586–3616.

Madura, J., J. Briggs, R. Wade, M. Davis, B. Luty, A. Ilin, J. Antosiewicz, M. Gilson, B. Bagheri, L. Scott, and J. McCammon. 1995. Electrostatics and diffusion of molecules in solution: simulation with the University of Houston Brownian Dynamics Program. *Comp. Phys. Comm.* 91:57–67.

Markussen, J., S. Havelund, P. Kurtzhals, A. S. Andersen, J. Halvstrøm, E. Hasselager, U. D. Larsen, U. Ribel, L. Schäffer, K. Vad, and I. Jonassen. 1996. Soluble, fatty acid acylated insulins bind to albumin and show protracted action in pigs. *Diabetologia.* 39:281–288.

Marrink, S., and A. Mark. 2001. Effect of undulations on surface tension in simulated bilayers. *J. Phys. Chem. B.* 105:6122–6127.

Meijer, A. B., R. B. Spruijt, C. J. A. M. Wolfs, and M. A. Hemminga. 2001. Membrane-anchoring interactions of M13 major coat protein. *Biochemistry.* 40:8815–8820.

Mouritsen, O. G., and M. Bloom. 1984. Mattress model of lipid protein interactions in membranes. *Biophys. J.* 46:141–153.

Mouritsen, O. G., and M. Bloom. 1993. Models of lipid protein interactions in membranes. *Annu. Rev. Biophys. Biomol. Struct.* 22:145–171.

Mouritsen, O. G., B. Damman, H. C. Fogedby, J. H. Ipsen, C. Jeppesen, K. Jørgensen, J. Risbo, M. C. Sabra, M. M. Sperotto, and M. J. Zukermann. 1995. The computer as a laboratory for the physical chemistry of membranes. *Biophys. Chem.* 55:55–66.

Mouritsen, O. G., and M. Sperotto. 1993. Thermodynamics of lipid-protein interactions in lipid membranes: the hydrophobic matching condition. *In* Thermodynamics of Membrane Receptors and Channels. M. Jackson, editor. CRC Press, Boca Raton, FL.

Murray, D., A. Arbuzova, B. Honig, and S. McLaughlin. 2002. The role of electrostatic and nonpolar interactions in the association of peripheral proteins with membranes. *Curr. Topics Membr.* 52:271–302.

Nagle, J. R., S. Zhang, S. Tristam-Nagle, W. Sun, H. Petrache, and R. M. Suter. 1996. X-ray structure determination of fully hydrated L_α dipalmitoylphosphatidylcholine. *Biophys. J.* 70:1419–1431.

Pedersen, T. B., M. Sabra, S. Frokjaer, O. G. Mouritsen, and K. Jørgensen. 2001a. Association of acylated cationic decapeptides with DPPS-CPPC lipid membranes. *Chem. Phys. Lipids.* 113:83–95.

Pedersen, T. B., M. Sabra, S. Frokjaer, O. G. Mouritsen, and K. Jørgensen. 2001b. Association of an acylated model peptide with DPPC-DPPS lipid membranes. *Int. J. Pharma.* 214:77–81.

Peters, G. H., T. M. Frimurer, J. N. Andersen, and O. H. Olsen. 1999. Molecular dynamics simulations of protein-tyrosine phosphatase 1b. I. Ligand-induced changes in the protein motions. *Biophys. J.* 77:505–515.

Schiffer, M., C.-H. Chang, and F. J. Stevens. 1992. The functions of tryptophan residues in membrane proteins. *Prot. Eng.* 5:213–214.

Schlenkrich, M., J. Brickmann, A. MacKerell, Jr., and M. Karplus. 1996. Empirical potential energy function for phospholipids: criteria for parameter optimization and applications. *In* Biological Membranes: A Molecular Perspective from Computation and Experiment. K. M. Merz and B. Roux, editors. Birkhauser, Boston, MA. 31–81.

Sham, Y., Z. Chu, and A. Warshel. 1997. Consistent calculations of pK_as of ionizable residues in proteins: semimicroscopic and microscopic approaches. *J. Phys. Chem.* 101:4458–4472.

Stryer, L. 1988. Biochemistry, 3rd Ed. Freedman, New York.

Tieleman, D. P., and H. J. C. Berendsen. 1996. Molecular dynamics simulations of a fully hydrated dipalmitoylphosphatidylcholine bilayer with different macroscopic boundary conditions and parameters. *J. Chem. Phys.* 105:4871–4880.

Tieleman, D. P., and H. J. C. Berendsen. 1998. A molecular dynamics study of the pores formed by *Escherichia coli* OmpF porin in a fully hydrated palmitoyloleoylphosphatidylcholine bilayer. *Biophys. J.* 74:2786–2801.

Tieleman, D. P., H. J. C. Berendsen, and M. S. P. Sansom. 1999. An alamethicin channel in a bilayer: molecular dynamics simulations. *Biophys. J.* 76:1757–1769.

Tuominen, E. K. J., C. J. A. Wallace, and P. K. J. Kinnunen. 2002. Phospholipid-cytochrome c interaction. Evidence for the extended lipid anchorage. *J. Biol. Chem.* 277:8822–8826.

van Gunsteren, W. F., and H. J. C. Berendesen. 1987. GROMOS87 Manual. BIOMOS BV, Groningen, The Netherlands.

van Gunsteren, W. F., and H. J. C. Berendesen. 1996. Biomolecular Simulation: The GROMOS96 Manual and User Guide. BIOMOS/ Hochschuleverlag AG and der ETH, Zürich, Switzerland; Groningen, The Netherlands.

White, S. H., and W. C. Wimley. 1998. Hydrophobic interactions of peptides with membrane interfaces. *Biochim. Biophys. Acta.* 1376:339–352.

You, T., and D. Bashford. 1995. Conformation and hydrogen ion titration of proteins: a continuum electrostatic model with conformational flexibility. *Biophys. J.* 69:1721–1733.

Zhang, Y., S. E. Feller, B. R. Brooks, and R. W. Pastor. 1995. Computer simulation of liquid/liquid interfaces. I. Theory and application to octane/ water. *J. Chem. Phys.* 103:10252–10266.